nature communications

Article

https://doi.org/10.1038/s41467-025-64002-z

Structural insights into the mechanism of activation and inhibition of the prostaglandin D2 receptor 1

Received: 10 March 2025

Accepted: 4 September 2025

Published online: 08 October 2025

Check for updates

Behnaz Davoudinasab[1,2], Aleksey Raskovalov[1,2,6], Woojin Lee[2,3,6], Donggyun Kim[1,2], Heesoo Kim[4], Jordy Homing Lam[2,3], Gye Won Han[2], Vsevolod Katritch[1,2,3,5] ✉ & Vadim Cherezov[1,2,5] ✉

The prostaglandin D2 receptor 1 (DP1), a member of the prostanoid G protein-coupled receptor (GPCR) family, plays critical roles in allergic responses, sleep regulation, immune modulation, and vasodilation. Here, we present five high-resolution cryo-electron microscopy (cryo-EM) structures of the human DP1 receptor, including an apo structure, two inactive state structures bound to two different inverse agonists developed by ONO Pharmaceutical, and two active state structures in complex with the G_s protein and bound to the endogenous agonist PGD2 and its selective derivative BW245C. Structural analysis, complemented by molecular dynamics simulations and site-directed mutagenesis, reveals key residues involved in ligand recognition and suggests a distinct activation mechanism for DP1, which lacks most of the conserved class A GPCR motifs. Notably, the unique residue K76 within the conserved sodium pocket acts as a major activation switch, while amphiphilic helix 8 adopts an unconventional orientation essential for receptor function. These findings offer valuable insights into the structure and function of prostanoid receptors and may facilitate the development of therapeutics targeting DP1.

Prostaglandin D2 (PGD2) is a vital bioactive lipid derived from arachidonic acid through the cyclooxygenase (COX) pathway. It plays significant roles in various physiological and pathological processes, including sleep induction, body temperature regulation, and nociception in the central nervous system[1–3]. Additionally, PGD2 is a major mediator in allergic reactions and inflammation within the immune system and serves as a potent inhibitor of platelet aggregation in the vascular system[4–6]. PGD2 exerts its effects primarily through two G protein–coupled receptors (GPCRs), DP1 and DP2 (also known as CRTH2)[7]. DP1 is predominantly expressed in cells involved in allergic and inflammatory responses, including mast cells, basophils, eosinophils, airway epithelial cells, vascular endothelial cells, and mucus-secreting goblet cells in the nasal and colonic mucosa[8,9]. DP2 is similarly expressed mainly in immune cells, including eosinophils, mast cells, and group 2 innate lymphoid cells (ILC2s)[10–12].

In addition to PGD2, other prostaglandins such as PGE2 and PGF2α, prostacyclin PGI2, and thromboxane A2 (TXA2) are also metabolized through COX pathways[13–15]. Their effects in humans are primarily mediated through nine prostanoid receptors: DP1 and DP2 for PGD2, 4 subtypes of PGE2 receptors (EP1 to EP4), the FP receptor for PGF2α, the IP receptor for PGI2, and the TP receptor for TXA2[16]. Notably, DP2 belongs to the gamma branch of the class A GPCR phylogenetic tree, unlike DP1 and other prostanoid receptors that are clustered in the α branch[17].

In humans, PGD2 is released in extensive quantities by activated mast cells in response to allergic stimuli[4,18,19]. Therefore, elevated levels

[1]Department of Chemistry, University of Southern California, Los Angeles, CA, USA. [2]Bridge Institute, University of Southern California, Los Angeles, CA, USA. [3]Department of Quantitative and Computational Biology, University of Southern California, Los Angeles, CA, USA. [4]Department of Biological Sciences, University of Southern California, Los Angeles, CA, USA. [5]Center for New Technologies in Drug Discovery and Development, University of Southern California, Los Angeles, CA, USA. [6]These authors contributed equally: Aleksey Raskovalov, Woojin Lee. ✉e-mail: katritch@usc.edu; cherezov@usc.edu

of PGD2 are promptly detected in bronchial lavage fluid following allergen exposure in patients with asthma[20]. Activation of DP2 by PGD2 leads to bronchoconstriction and type 2 inflammation[21–24], while activation of DP1 by PGD2 inhibits dendritic cell migration to lymph nodes, enhances regulatory T-cell function, and induces eosinophil apoptosis, contributing to resistance against asthma[25,26].

DP1 is a G_s-coupled receptor that mediates many of the central nervous system and immune responses attributed to PGD2. Activation of DP1 leads to an elevation of intracellular cyclic adenosine monophosphate (cAMP), which causes downstream effects such as relaxation of smooth muscles, inhibition of platelet aggregation, and modulation of immune cell activity. This receptor is implicated in various allergic and inflammatory conditions, including asthma, allergic rhinitis, and atopic dermatitis[26,27].

Several non-selective prostanoid receptor agonists, such as iloprost, treprostinil, and alprostadil (PGE1), which activate DP1 along with other prostanoid receptors, have been approved by the FDA for various indications[28–30]. However, so far none of DP1-selective ligands, including laropiprant (MK-0524), asapiprant (BGE-175), ONO-4053, and TS-022, tested in clinical trials, have successfully completed the process due to challenges in efficacy and safety. In general, DP1 antagonism may have merit in the treatment of asthma, rhinitis, and conjunctivitis, while DP1 agonism is explored for the treatment of pulmonary hypertension, atopic dermatitis, and obesity. A deeper understanding of the mechanisms of action of selective DP1 antagonists and agonists is essential to develop effective treatments for these conditions, while minimizing side effects associated with non-specific modulation of the COX pathway.

Recent advances in X-ray crystallography and single-particle cryogenic electron microscopy (cryo-EM) have revolutionized our understanding of GPCR structures and their molecular mechanisms, greatly facilitating the design of selective ligands[31–36]. Although significant progress has been made in determining structures of both inactive and active states of prostanoid receptors, the full activation mechanism of these receptors is still ambiguous and not fully understood. Among the nine known prostanoid receptors, active state structures have been determined for EP2[37], EP3[38–41], EP4[41,42], FP[43–45], TP[45], IP[46], and DP2[47], while inactive state structures have been resolved only for TP[48], EP4[49], and DP2[50,51].

Here, we present five high-resolution cryo-EM structures of the human DP1 receptor in both active and inactive states (Fig. 1a, b and Supplementary Table 1). Two of these structures depict the fully active DP1 receptor in complex with its cognate G_s heterotrimer, bound to its endogenous agonist PGD2 and its selective synthetic agonist BW245C. Additionally, we present three inactive state structures of DP1, including the receptor in its apo form as well as bound to two synthetic DP1 selective antagonists developed by ONO Pharmaceutical. These structural characterizations, combined with functional analysis of mutated receptors and molecular modeling, provide detailed insights into the molecular mechanisms of DP1 receptor activation and inhibition, offering a valuable framework for the rational design of selective DP1 modulators with potential therapeutic applications.

Results

Cryo-EM structures of DP1 in the inactive state

To stabilize the inactive state of the human DP1 receptor, we replaced the third intracellular loop (ICL3) with a thermostabilized apocytochrome b562 fusion protein (bRIL)[52] and introduced three-point mutations, C130$^{3.50}$R, H263$^{6.33}$A, and D319$^{7.49}$N (superscripts refer to the Ballesteros-Weinstein numbering scheme[53] for Class A GPCRs), which improved the yield of the purified receptor and its thermostability (Supplementary Figs. 1–3). Two of these mutations, C130$^{3.50}$R and D319$^{7.49}$N, also decreased the potency of PGD2 in ONE-GO G_s protein activation assays[54,55] (Fig. 2g, Supplementary Fig. 4, and Supplementary Table 2). While inserting bRIL into the ICL3 or N-terminus of GPCRs is a well-established method for facilitating crystal contacts in X-ray crystallography[52], bRIL and its synthetic antibody have also been employed as fiducial markers in single-particle cryo-EM[56–58]. To enhance the rigidity between the bRIL fusion protein and DP1, we optimized junction sites by inserting bRIL between ICL3 residues Q233 and L258 with a short linker (ERARSTL) added before L258, as inspired by the construct designs from previously determined GPCR structures[34,57]. Using this approach, we determined three structures of the inactive state of the DP1$_{ICL3}$bRIL receptor in complex with an anti-bRIL Fab antibody (BAG2) and a Fab stabilizing nanobody (Nb) by single-particle cryo-EM. These structures were captured in its apo form (without adding a ligand) and bound to two different antagonists developed by ONO Pharmaceutical, ONO3030297 and ONO2550289, at nominal resolutions of 2.84 Å, 2.89 Å, and 2.89 Å, respectively (Supplementary Figs. 5–7, Supplementary Table 1). The high-resolution cryo-EM density maps allowed us to build most regions of the DP1$_{ICL3}$bRIL-BAG2-Nb complex, encompassing residues 3 to 342 of DP1, except for the flexible ICL1 (residues 47–58) and truncated ICL3 (residues 234–257), bRIL, anti-bRIL Fab, and Nb. Maps obtained in the presence of ONO3030297 and ONO2550289 show strong density for the ligands (Fig. 1a). Interestingly, the apo form map also displays some density in the orthosteric binding pocket, suggesting that the pocket may be occupied by a native lipid-like molecule captured from the cell.

The overall architecture of the inactive state of DP1 adopts the canonical seven-transmembrane helical domain (7TM) in its inactive conformation (Fig. 1c), without any significant outward displacement of the cytoplasmic end of TM6, typically associated with class A-GPCR activation[59]. The orientation of the C-terminal amphiphilic helix 8 (H8) is directed toward TM6, which differs from the classical configuration of H8 oriented towards TM1 in most class A-GPCRs and will be discussed further in more detail.

The extracellular entrance in the ligand binding pocket of DP1 is tightly capped by the extracellular loop 2 (ECL2), which folds into a long β-hairpin stabilized by a highly conserved disulfide bond between C105$^{3.25}$ and C183^{ECL2} (Fig. 1c), similar to other prostanoid receptors. The pocket, however, is open to the membrane via a gap between TM1 and TM7 (Fig. 2a, b). Moreover, DP1 features an additional disulfide bond in the extracellular region between the N-terminus (C8) and C178^{ECL2}. Cysteines at similar positions are present in EP2 and IP, however, the N-terminus is not visible in EP2 structures[37], while no disulfide bonds were modeled in the IP receptor[46]. Among other prostanoid receptors, two disulfide bonds have been also observed in TP[48], where the second disulfide bond forms between the N terminus and the extracellular tip of TM3 (C11-C102$^{3.22}$). Mutations of these two TM3 cysteines (C$^{3.22}$S and C$^{3.25}$S) and the conserved ECL2 cysteine (C^{ECL2}S) in TP abolished the binding of an antagonist[48], suggesting that both disulfide bonds contribute towards shaping the binding pocket. In DP1, this double-layer capping effectively occludes the orthosteric binding site and may limit the access of the ligand from the extracellular side. Both the lipid nature of the endogenous agonist and the double-layer capping suggest that the gap between TM1 and TM7 could serve as the potential access route to the orthosteric binding site (Fig. 2a, b), a pathway also proposed in other lipid receptor structures, such as S1P1 and rhodopsin. Our MD simulations indicate that the ECL access to the orthosteric site remains closed, while the TM1-TM7 gap stays predominantly open, suggesting this gap as a potential ligand entry point—an observation similar to the one made in the metadynamics study of EP4[49].

The two DP1$_{ICL3}$bRIL structures bound to ONO2550289 and ONO3030297 are highly similar, with a Cα root mean square deviation (RMSD$_{Cα}$) of 0.52 Å within the 7TM bundle. The apo state DP1 structure, however, shows slight differences compared to these two inactive structures, with RMSD$_{Cα}$ of 0.75 Å and 0.66 Å within 7TM compared with structures bound to ONO2550289 and ONO3030297, respectively. In the apo

https://doi.org/10.1038/s41467-025-64002-z

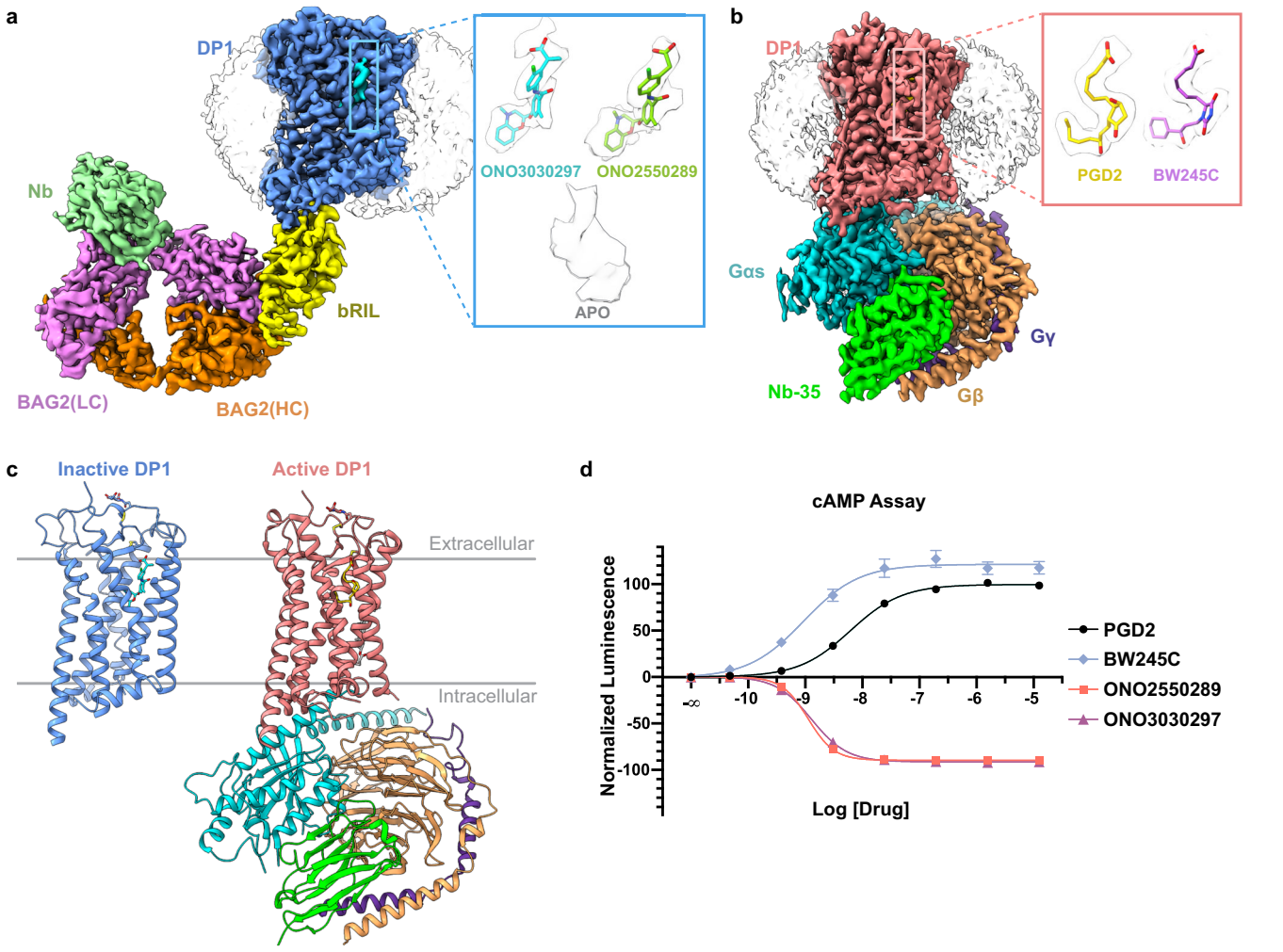

Fig. 1 | Cryo-EM DP1 structures in the inactive and active G_s protein bound states. a Cryo-EM density of the inactive state $DP1_{ICL3}$bRIL construct (DP1—blue, bRIL—yellow) bound to the inverse agonist ONO3030297 (cyan) and in complex with the anti-bRIL Fab (BAG2, heavy chain—orange, light chain—pink) and stabilizing nanobody (Nb, light green). The insert shows EM densities in the ligand binding pocket for ONO3030297, ONO2550289, and APO receptor. **b** Cryo-EM density of DP1 (salmon) bound to PGD2 (gold) and in complex with heterotrimeric G_s protein ($G\alpha_s$—cyan, Gβ—sand, Gγ—violet) and nanobody Nb-35 (green). The insert shows EM densities in the ligand binding pocket for agonists PGD2 and BW245C. The ligands in (**a**–**c**) are shown as sticks with carbon atoms colored in cyan (ONO3030297), chartreuse (ONO2550289), gold (PGD2) or violet (BW245C). **c** Structures of DP1 in the inactive state and in the active Gs protein-bound states. Two gray lines indicate membrane boundaries as provided by the Orientation of Proteins in Membranes (OPM) database. **d** Cellular cAMP production assay with transiently transfected WT DP1. The agonist data are normalized to the basal signal (set at 0%) and the maximal PGD2-induced signal (set at 100%). The inverse agonist data are normalized to the basal signal (set at 0%) and the signal from the empty vector-transfected cells (set at −100%). Data points correspond to means ± SEM for three biologically independent experiments conducted in triplicates. The corresponding E_{max} and EC_{50} values are shown in Supplementary Table 3. Source Data are provided as a Source data file.

structure, the extracellular part of TM1 shifts toward TM7 by 1.5–2 Å while TM2 shifts outwards by 2–3 Å, causing the distance between TM1 and TM2 to increase, while the gap between TM1 and TM7 decreases (Supplementary Fig. 8a, b).

The unique among class A GPCR lysine residue $K76^{2.54}$, located deep in the 7TM bundle, plays a key role in stabilizing the inactive state of DP1. In both antagonist complexes, it forms a salt bridge to $D72^{2.50}$ (Fig. 2c), a highly conserved residue in the sodium pocket of class A GPCRs[60,61]. The salt bridge remains stable in MD simulations of the inactive receptor (Supplementary Fig. 9a, b). Although all 15 residues of the sodium pocket are fully conserved in DP1, the binding of sodium to $D72^{2.50}$ is apparently blocked by the positively charged $K76^{2.54}$ occupying the pocket. This is supported by MD simulations where sodium ions do not enter the pocket in any of the nine MD simulations of the apo state receptor (Supplementary Fig. 10), unlike those observed in other GPCRs[62].

Antagonist binding pocket

Though commonly referred to as antagonists, both ONO compounds fully inhibit the basal activity of DP1 in cAMP accumulation assays and therefore act as inverse agonists with EC50 values of 1.1 nM and 1.3 nM for ONO2550289 and ONO3030297, respectively (Fig. 1d and Supplementary Table 3). Both ONO ligands share a similar chemical structure, featuring a central meta-xylene ring connected via an amide bond to a chlorphenylacetic group on one side and via an ether bond to a dimethyl-1,4-benzoxazine group on the other side (Fig. 2e, f). However, ONO3030297 includes an additional cyclopropane group and demonstrates slightly different effects when bound to DP1. The $DP1_{ICL3}$bRIL-ONO3030297 complex exhibits a 2 °C increase in the melting temperature compared to ONO2550289 (Supplementary Fig. 2b). Additionally, a substantial proportion of dimers is observed for $DP1_{ICL3}$bRIL-ONO3030297, whereas $DP1_{ICL3}$bRIL-ONO2550289 remains mostly monomeric, based on the final size exclusion

https://doi.org/10.1038/s41467-025-64002-z

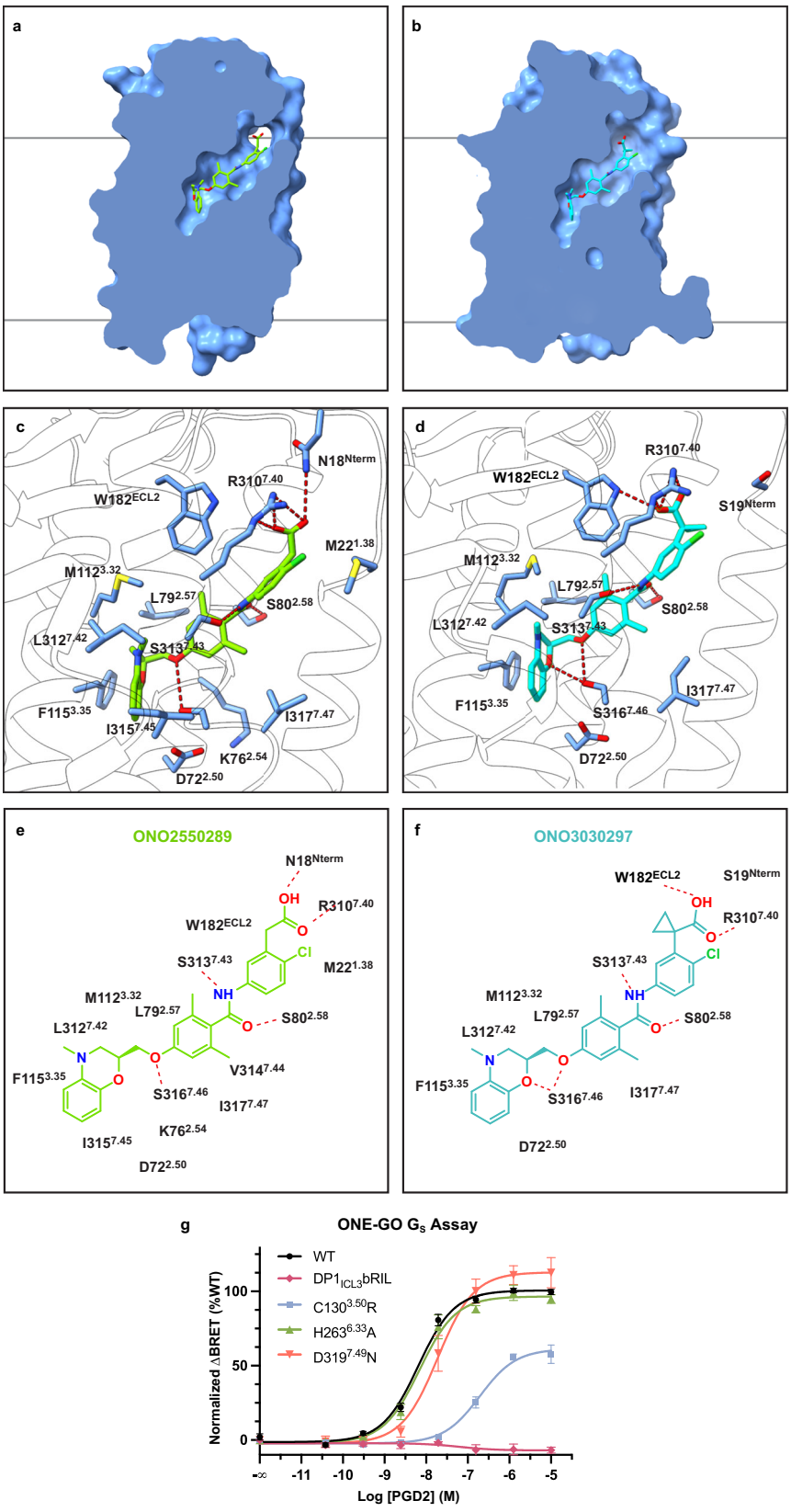

chromatography (SEC) curve (Supplementary Fig. 3e) and cryo-EM 2D particle classification (Supplementary Figs. 6c and 7c).

Both ONO compounds occupy the same predominantly hydrophobic binding pocket, formed by residues from TMs 1, 2, 3, 7, and ECL2, following a path from the ECL region to as deep as the entrance to the conserved sodium binding pocket (Fig. 2a–d and Supplementary Fig. 11a, b). However, overlaying the two DP1 structures reveals a slight difference in the conformations of the ONO inverse agonists within the orthosteric binding pocket. In both structures, the carboxylic group of the ligand primarily makes a salt bridge with the sidechain of R310$^{7.40}$, a residue fully conserved in prostanoid receptors (Fig. 2c, d). Additionally, the carboxylic group of ONO2550289 forms

Fig. 2 | Ligand binding pocket in the inactive DP1 and recognition of inverse agonists. a, **b** Cross-section through the receptor showing the ligand bound site and bound ligands for ONO2550289 (**a**) and ONO3030297 (**b**). Two gray lines indicate membrane boundaries as provided by the Orientation of Proteins in Membranes (OPM) database. **c**, **d** Details of DP1 residues' interactions with ONO2550289 (**c**) and ONO3030297 (**d**). Hydrogen bonds and salt bridges are shown as red dashed lines. The ligands in (**a**–**d**) are shown as sticks with carbon atoms colored in chartreuse (ONO2550289) or cyan (ONO3030297). **e**, **f** Schematics of DP1 residues' interactions with ONO2550289 (**e**) and ONO3030297 (**f**). Hydrogen bonds and salt bridges are shown in red dashed lines. **g** ONE-GO G_s signaling assay comparing the concentration-response signal induced by PGD2 at WT DP1 with the inactive cryo-EM construct ($DP1_{ICL3}$bRIL) and the inactive state stabilizing mutants C130$^{3.50}$R, H263$^{6.33}$A, and D319$^{7.49}$N. The data are normalized to the basal signal (set at 0%) and the maximal PGD2-induced signal at WT DP1 (set at 100%). Data points correspond to means ± SEM for three biologically independent experiments conducted in triplicates. The corresponding E_{max} and EC_{50} values are shown in Supplementary Table 2. Source Data are provided as a Source data file.

an additional hydrogen bond with N18^{Nterm}, while the one of ONO3030297 with W182^{ECL2}. Residues A20$^{1.36}$, M22$^{1.38}$, and L26$^{1.42}$ make hydrophobic interactions with the chlorophenylacetic ring. The cyclopropane group of ONO3030297 introduces additional hydrophobic interactions with S19^{Nterm}, G23$^{1.39}$, V83$^{2.61}$, and L84$^{2.62}$ residues and pushes the N-terminal stretch of residues 16-21 widening the putative ligand entrance gap.

The amide group of both ligands interacts with S80$^{2.58}$ and S313$^{7.43}$ via hydrogen bonding. Additionally, in the DP1-ONO3030297 structure, S316$^{7.46}$ establishes hydrogen bonds with both the ether oxygen and the oxygen in the heterocyclic group of the ligand, while in the DP1-ONO2550289 structure, only the ether oxygen is within the hydrogen bond distance from S316$^{7.46}$. Despite this difference, the hydrophobic interactions around the heterocyclic region (2,3-dihydro-1,4-benzoxazine) of the ONO compounds and the surrounding residues remain largely conserved. In both ONO-bound structures, the heterocycles of the ligands occupy a compact pocket formed by residues G75$^{2.53}$, L79$^{2.57}$, M112$^{3.32}$, F115$^{3.35}$, S119$^{3.39}$, L312$^{7.42}$, and I315$^{7.45}$.

Our MD simulations of DP1 in complex with ONO3030297 supported the stability of these interactions and the key role of polar interactions with R310$^{7.40}$, S80$^{2.58}$, and S313$^{7.43}$ side chains (Supplementary Fig. 12), as well as suggested water-mediated interactions between the morpholine nitrogen of ONO3030297 and backbone atoms of L312$^{7.42}$, S313$^{7.43}$, I315$^{7.45}$, and both backbone and sidechain of S316$^{7.46}$ (Supplementary Fig. 13).

Cryo-EM structures of DP1 in the active state

To facilitate the expression and purification of the human wild-type (WT) DP1 receptor, we introduced a FLAG tag at the N-terminus immediately after the hemagglutinin signal peptide, and a cleavable enhanced green fluorescent protein (eGFP) with an 8×His tag at the C-terminus of the canonical DP1 gene sequence (UniProt Q13258). The resulting DP1 construct was then co-expressed with the dominant-negative form of $G\alpha_s$ (DNG_s)[63], $G\beta_1$, and $G\gamma_2$ in *Spodoptera frugiperda* (*Sf9*) insect cell. The DP1-G_s complex was stabilized by adding an agonist (PGD2 or BW245C) and a nanobody 35 (Nb35)[64] in the presence of apyrase, enabling efficient assembly and generating highly homogenous complex samples suitable for structural studies (Supplementary Fig. 14). The structures of the DP1-G_s-Nb35 complex bound to PGD2 and BW245C were determined by single-particle cryo-EM at nominal resolutions of 2.68 Å and 2.45 Å, respectively (Fig. 1b and Supplementary Table 1). The high-resolution cryo-EM density maps enabled accurate model building for the DP1-G_s-Nb35 complex containing residues 3 to 338 of DP1 except for the flexible ICL1 (residues 48–57) and ICL3 (residues 236–254), most residues of the G_s protein heterotrimer except for the flexible α-helical domain of $G\alpha_s$ protein, and Nb35 (Supplementary Figs. 15, 16). Meanwhile, agonists PGD2 and BW245C were modeled into well-defined densities in the DP1 ligand-binding pocket (Fig. 1b and Supplementary Fig. 11c, d). DP1-G_s complexes bound to PGD2 and BW245C are very similar, with $RMSD_{C\alpha}$ of just 0.15 Å across the 7TM bundle, with some local variations in the side chains. Both complexes display an essentially identical interface between the receptor and G_s protein.

The active DP1 structure reveals an outward displacement of the cytoplasmic end of TM6 (Cα atom of E260$^{6.30}$) by ~5 Å relative to the inactive DP1 structure. Such a modest activation-related shift of TM6 for a G_s-coupled receptor appears to be a feature of prostanoid receptors. Additionally, TM5 shifts closer to TM6 and TM7 moves inward—both are characteristic features of activation observed in class A GPCRs. The amphiphilic H8 becomes shorter and more disordered, while maintaining its interaction with TM6.

The active state of the human DP1 receptor shares high structural similarity with the EP2 (7CX2) and IP (8X79) receptors (37% and 30% sequence identity) with an $RMSD_{C\alpha}$ of 0.80 Å and 0.97 Å across the 7TM bundle, respectively (Supplementary Fig. 17). A comparative analysis of the active DP1-Gs structure with other active prostanoid receptor complexes reveals a conserved overall architecture across these receptors, except for the orientation of H8, which varies substantially between them (Supplementary Table 4). This distinct structural feature may have implications for the distinct functional properties of the DP1 receptor.

Agonist binding pocket

The endogenous agonist PGD2 and its synthetic derivative, the highly potent selective agonist BW245C, with EC50 values in cAMP assays of 6.2 nM and 1.1 nM, respectively (Fig. 1d and Supplementary Table 3), bind within the orthosteric pocket formed by TMs 1, 2, 3, 7, and ECL2, consisting of three subpockets accommodating the α-chain, the core ring, and the ω-chain of the ligands (Fig. 3). The pocket is almost fully occluded with a narrow solvent-accessible channel, similar to the active-state of EP2. In both the PGD2- and BW245C-bound structures, the negatively charged carboxy end of the α-chain forms a strong salt bridge with the conserved residue R310$^{7.40,}$ in addition to hydrogen bonds with the conserved residues T181^{ECL2} and Y87$^{2.65}$. Mutations R310$^{7.40}$A, T181^{ECL2}, and Y87$^{2.65}$A substantially decreased the potency of PGD2 in our ONE-GO assays (Fig. 3g and Supplementary Table 2). The conserved in prostanoid receptors hydrophobic residues W182^{ECL2}, M112$^{3.32}$, L306$^{7.36}$, and L309$^{7.39}$ and non-conserved hydrophobic residue V83$^{2.61}$ interact with the hydrophobic part of the α-chain. Accordingly, mutations W182^{ECL2}A, M112$^{3.32}$A, and L306$^{7.36}$A reduced the potency of PGD2 (Fig. 3g). Our MD simulations further support the highly dominant salt bridge between R310$^{7.40}$ and the carboxy group (present >95% of time) and suggest only modest contributions of direct polar interactions for Y87$^{2.65}$ (25%) and T181^{ECL2} (10%) (Supplementary Fig. 18a).

The carbonyl group on the core ring of both ligands make a hydrogen bond with K76$^{2.54}$ and possibly a polar or water mediated interaction with S80$^{2.58}$. In addition, the amino group in the core ring of BW245C engages in a hydrogen bond with the backbone carbonyl of G23$^{1.39}$. In agreement, both mutations, S80$^{2.58}$A and K76$^{2.54}$A, decreased the potency of PGD2 in our ONE-GO assays (Fig. 3g). Interestingly, G23$^{1.39}$A slightly increased the potency of PGD2, likely due to a moderate stabilization effect of the alanine side chain on PGD2 binding. Furthermore, the MD analysis of heavy atom interactions between PGD2 and the binding pocket residues (Supplementary Fig. 18) aligns qualitatively with experimental mutation studies of the PGD2 binding pocket (Fig. 3e, g). Both computational and experimental results support the importance of these residues in PGD2 binding interactions. Note that MD simulations suggest additional water-mediated polar interactions of PGD2 hydroxyl groups: 9-OH with S80$^{2.58}$ and S313$^{7.43}$, and 15-OH with Y203$^{5.41}$ of DP1 (Supplementary Fig. 19).

https://doi.org/10.1038/s41467-025-64002-z

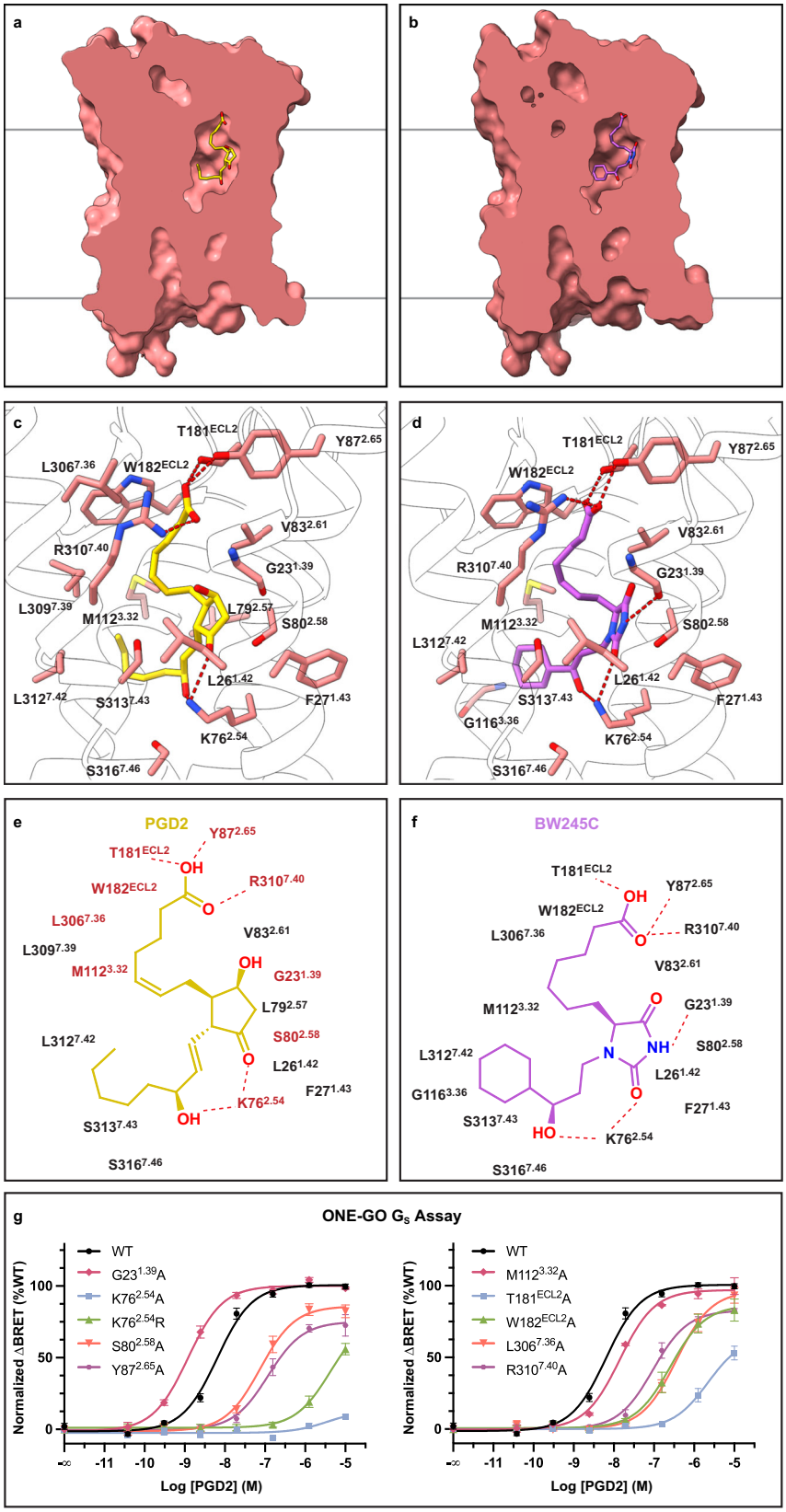

In addition to the similar hydrophobic interactions of the ω-chain of PGD2 and BW245C with neighboring residues including L79$^{2.57}$, G75$^{2.53}$, L312$^{7.42}$, BW245C contains a bulky cyclohexane group at the end of its ω-chain which allows for a tighter fit into the hydrophobic subpocket, potentially contributing to the enhanced potency of BW245C compared to PGD2.

Endogenous ligand binding in prostanoid receptors, excluding DP2, is primarily driven by interactions between the ligand's carboxy

Fig. 3 | Ligand binding pocket in the active DP1 and recognition of agonists. **a**, **b** Cross-section through the receptor showing the ligand bound site and bound ligands for PGD2 (**a**) and BW245C (**b**). Two gray lines indicate membrane boundaries as provided by the Orientation of Proteins in Membranes (OPM) database. **c**, **d** Details of DP1 residues' interactions with PGD2 (**c**) and BW245C (**d**). Hydrogen bonds and salt bridges are shown as red dashed lines. The ligands in (**a**–**d**) are shown as sticks with carbon atoms colored in gold (PGD2) or violet (BW245C). **e**, **f** Schematics of DP1 residues' interactions with PGD2 (**e**) and BW245C (**f**). Hydrogen bonds and salt bridges are shown in red dashed lines. Residues that showed significant effects in ONE-GO G_s signaling assays are colored in red. **g** ONE-GO G_s signaling assay comparing the concentration-response signal induced by PGD2 at WT DP1 with binding pocket residue mutants. The data are normalized to the basal signal (set at 0%) and the maximal PGD2-induced signal at WT DP1 (set at 100%). Data points correspond to means ± SEM for three biologically independent experiments conducted in triplicates. The corresponding E_{max} and EC_{50} values are shown in Supplementary Table 2. Source Data are provided as a Source data file.

group on the α-chain and three conserved residues: $R^{7.40}$, $Y^{2.65}$, and T/S^{ECL2}, which stabilize the ligand through a network of electrostatic forces, hydrogen bonds, and polar contacts. In addition, conserved hydrophobic residues $M/L^{3.32}$ and $L/F^{7.36}$ along the aliphatic region of the α-chain further stabilize the binding.

Mechanism of DP1 activation

Activation of the DP1 receptor is driven by agonist-induced conformational changes within the ligand-binding pocket. Specifically, the extracellular part of TM1 shifts towards TM7 by 4–5 Å, while TM7 moves outward and down by around 2 Å, closing the gap between these two helices (Fig. 4a, b). A critical conformational change occurs at $W182^{ECL2}$, causing $L309^{7.39}$ to shift downward (Fig. 4c). The $W182^{ECL2}$A mutation was found to reduce PGD2 potency in ONE-GO assays (Fig. 3g and Supplementary Table 2).

The DP1 receptor lacks the classical $W^{6.48}$ toggle switch present in many class A GPCRs. This residue is replaced with $S278^{6.48}$ that forms a hydrogen bond with the mainchain carbonyl of $F274^{6.44}$ stabilizing a kink in TM6. Furthermore, the canonical P-I-F motif is substituted with $L212^{5.50}$-$T120^{3.40}$-$F274^{6.44}$ in DP1. However, these residues in DP1 do not interact with each other. Instead, the role of the activation switch in DP1 can be played by an alternative motif $T214^{5.52}$-$L123^{3.43}$-$F274^{6.44}$ (Fig. 4d). During activation, the downward movement of $I315^{7.45}$ on TM7 prompts $F274^{6.44}$ to undergo a rotomeric switch in conjunction with a switch in $L123^{3.43}$ and a shift of $T214^{5.52}$ towards $L123^{3.43}$. This cascade of molecular switches enables the outward movement of the intracellular portion of TM6, a hallmark of receptor activation. The contribution of this motif into DP1 activation, however, remains unclear as the $F274^{6.44}$A mutation did not affect PGD2 induced signaling in ONE-GO assays (Fig. 4h).

Another important part of the activation mechanism is the sodium binding pocket, which exhibits high conservation in DP1 in both residue composition and structure, compared to other class A GPCRs[61]. In addition to the highly conserved $D72^{2.50}$, DP1 features a second acidic residue $D319^{7.49}$ within the pocket, a variant present in approximately 20% of non-olfactory class A receptors. Notably, the $D319^{7.49}$N mutation used in the inactive state construct reduced the PGD2 potency, indicating its functional relevance (Fig. 2g and Supplementary Table 2). Although a sodium ion coordinated by both the acidic side chains of $D^{2.50}$ and $D^{7.49}$ has been observed in the structures of several receptors[65–67], no such sodium ion was found in the pocket of our experimental inactive state structures of DP1 or in our MD simulations (Supplementary Fig. 10). Upon receptor activation, the sodium pocket undergoes major structural rearrangement. In the inactive state, the unique DP1 residue $K76^{2.54}$, absent in other class A GPCRs, makes a salt bridge with $D72^{2.50}$ and a hydrogen bond with $N34^{1.50}$ (Fig. 4e). Stability of these interactions is strongly supported by our MD simulations (Supplementary Fig. 9a, b). The positively charged primary amine of $K76^{2.54}$ occupies a position similar to that of sodium ions in other class A GPCRs and likely serves a similar role in stabilizing the receptor's inactive state. Upon agonist binding, the primary amine group of $K76^{2.54}$ repositions to interact directly with the carbonyl and hydroxyl groups of the agonist, while $D72^{2.50}$ forms a hydrogen bond with $D319^{7.49}$, making a distinct conformational shift in the sodium pocket. The $D72^{2.50}$N mutation increased the basal receptor activity in cAMP accumulation assays, while $K76^{2.54}$A completely abrogated PGD2 signaling in ONE-GO assays without affecting its basal activity (Fig. 3g, Supplementary Fig. 4, and Supplementary Table 2). The lack of changes in basal activity could be explained by a sodium ion replacing the amino group of $K76^{2.54}$A to maintain stability of the inactive state. The conformational shift of $K76^{2.54}$ from engaging in a salt bridge with $D72^{2.50}$ to hydrogen bonding with the agonist appears to function as a key activation switch, distinct to DP1. Interestingly, replacing $K76^{2.54}$ with another positively charged residue, arginine, substantially decreased the PGD2 potency in ONE-GO assays (Fig. 3g and Supplementary Table 2), likely due to steric constraints introduced by the bulky guanidine group of arginine. Notably, the ONO ligands possess hydrophobic groups that prevent $K76^{2.54}$ from adopting its "upward" orientation; instead, promoting a conformation in which this residue interacts with $D72^{2.50}$ and $N34^{1.50}$, stabilizing the inactive state and thus explaining their inverse agonism. In the apo state, the conformation of $K76^{2.54}$ is intermediate between the states observed in inverse agonist- and agonist-bound structures. Another notable feature, supported by strong EM density, is that in the active state, $D72^{2.50}$ and $D319^{7.49}$ are engaged in a strong polar interaction (3.0 Å, Fig. 4e) which is only energetically possible if one of these acidic side chains is protonated and thus uncharged. Protonation of $D^{2.50}$ upon activation has previously been proposed as a part of activation mechanism in class A GPCRs[68]. To assess the effect of $D72^{2.50}$ protonation, we conducted MD simulations of the active state DP1 with charged and protonated $D72^{2.50}$. Simulations with charged $D72^{2.50}$ showed a high frequency of $D72^{2.50}$-$K76^{2.54}$ salt bridge interactions (Fig. 4g, Supplementary Fig. 9c, d), which was not supported by the cryo-EM structure of the DP1 active state. In contrast, MD simulations with protonated $D72^{2.50}$ demonstrated an apparent switch of the $K76^{2.54}$ side chain from the salt bridge with $D72^{2.50}$ to interactions with the PGD2 carbonyl and hydroxy groups (Fig. 4g, Supplementary Fig. 9e, f), in agreement with the active-state cryo-EM structures. Thus, the MD simulations suggest that protonation of $D72^{2.50}$ is required for this dramatic conformational change in $K76^{2.54}$, likely serving as a key activation switch, specific to DP1.

On the intracellular side of the receptor, the conserved D(E)RY motif is replaced with $E129^{3.49}C130^{3.50}W131^{3.51}$. DP1 is the only prostanoid receptor, in which $R^{3.50}$ is not conserved. Note that the inactive state construct includes the $C130^{3.50}$R mutation, which strongly decreased basal activity of DP1 in cAMP accumulation assay and PGD2 potency in ONE-GO assay (Fig. 2g, Supplementary Fig. 4, and Supplementary Table 2). The inactive state structure confirms that $R130^{3.50}$ forms a classical ionic lock with $E260^{6.30}$, explaining the stabilizing effect of $C130^{3.50}$R in the inactive state DP1 construct (Fig. 4f). The NPxxY motif is replaced with DPxxF motif in DP1. The side chain of $F323^{7.53}$ rotates upon activation along with the backbone of TM7 and stabilizes the active state by hydrophobic interactions with $F61^{2.39}$, $L123^{3.43}$, $M126^{3.46}$, and $M270^{6.40}$. The mutation $F323^{7.53}$Y, restoring the DPxxY motif, has negligible effect on the PGD2 potency (Fig. 4h and Supplementary Table 2).

DP1-G_s interface

The re-arrangements of TM5, TM6, and TM7 on the cytoplasmic side upon agonist binding create a cavity to accommodate the α5 helix of the $G\alpha_s$ subunit (Fig. 5a, b). Unlike the wider cytoplasmic cavity in β_2AR-G_s[64] and other G_s coupled complexes, the DP1-G_s complex has a

https://doi.org/10.1038/s41467-025-64002-z

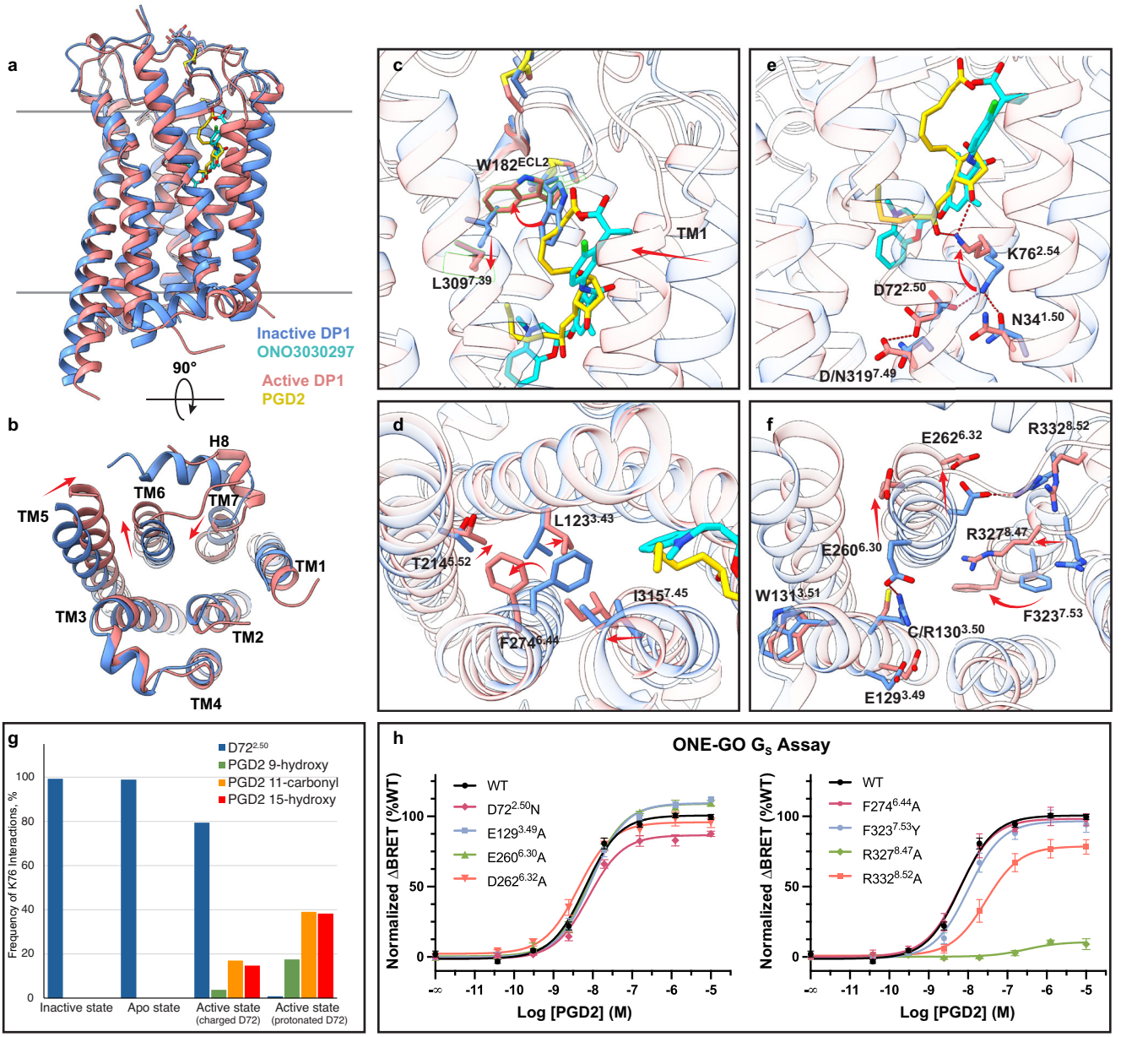

Fig. 4 | DP1 activation mechanism. a, **b** Comparison of the inactive (blue) and active (salmon) states of DP1, viewed within the plane of the membrane (**a**) and from the intracellular side (**b**). Red arrows indicate main conformational shifts of TMs on the intracellular side of the receptor. The membrane boundaries are shown in (**a**) as two gray lines. **c**–**f** Structural details of activation-related motifs in DP1, showing the ligand binding pocket (**c**), the $T^{5.52}$-$L^{3.43}$-$F^{6.44}$ motif (**d**), the sodium-binding site (**e**), the $EC^{3.50}W$ and $DP^{7.50}xxF$ motifs (**f**). The ligands in (**a**–**f**) are shown as sticks with carbon atoms colored in gold (PGD2) or cyan (ONO3030297). **g** MD analysis of $K76^{2.54}$ interactions with $D72^{2.50}$ and PGD2. **h** ONE-GO G_s signaling assay comparing the concentration-response signal induced by PGD2 at WT DP1 with activation-related mutants. The data are normalized to the basal signal (set at 0%) and the maximal PGD2-induced signal at WT DP1 (set at 100%). Data points correspond to means ± SEM for three biologically independent experiments conducted in triplicates. The corresponding E_{max} and EC_{50} values are shown in Supplementary Table 2. Source Data are provided as a Source data file.

narrower cavity due to the closer proximity of the TM3-TM6-TM7 bundle (Fig. 5c, d). To avoid steric clashes, the entire G_s heterotrimer rotates around the axis perpendicular to the membrane by ~15-20 degrees clockwise looking from the intracellular side with respect to the receptor, compared to β_2AR-G_s (Fig. 5b). Additionally, the α5 helix of $G\alpha_s$ extends toward TM1 of DP1, rather than turning towards TM6 as in β_2AR-G_s. Such an arrangement is common among prostanoid receptors[37,42,46].

The C-terminal residues $L394^{G.H5.26}$ and $L393^{G.H5.25}$ (superscript indicates the common Gα numbering (CGN) system[69]) of the α5 helix extend into a hydrophobic pocket formed by $L40^{1.56}$, $F61^{2.42}$, $Y62^{2.43}$, $V65^{2.46}$, and $I324^{7.54}$ on the cytoplasmic ends of TM1, TM2, and TM7 of DP1 (Fig. 5e, f). The backbone carbonyl of $Y391^{G.H5.23}$ on the α5 helix makes a hydrogen bond with $R327^{8.47}$ of DP1. The $R327^{8.47}$A mutation significantly reduces the potency of PGD2 by over 70-fold, suggesting this interaction is crucial for the recruitment of $G\alpha_s$ (Fig. 4h and Supplementary Table 2). The sidechain of $E392^{G.H5.24}$ on the α5 helix of $G\alpha_s$ interacts with the backbone nitrogen and carbonyl oxygen of $L258^{6.28}$, while $Q390^{G.H5.22}$ and $Y391^{G.H5.23}$ engage in hydrogen bonds with the conserved residue $E129^{3.49}$ of the (E/D)RY motif as well as $Y391^{G.H5.23}$ hydrogen bonds with $S133^{3.53}$ (Fig. 5e, f). The sidechain of $F138^{ICL2}$ is buried into a hydrophobic pocket formed by $I383^{G.H5.15}$, $R380^{G.H5.12}$,

https://doi.org/10.1038/s41467-025-64002-z

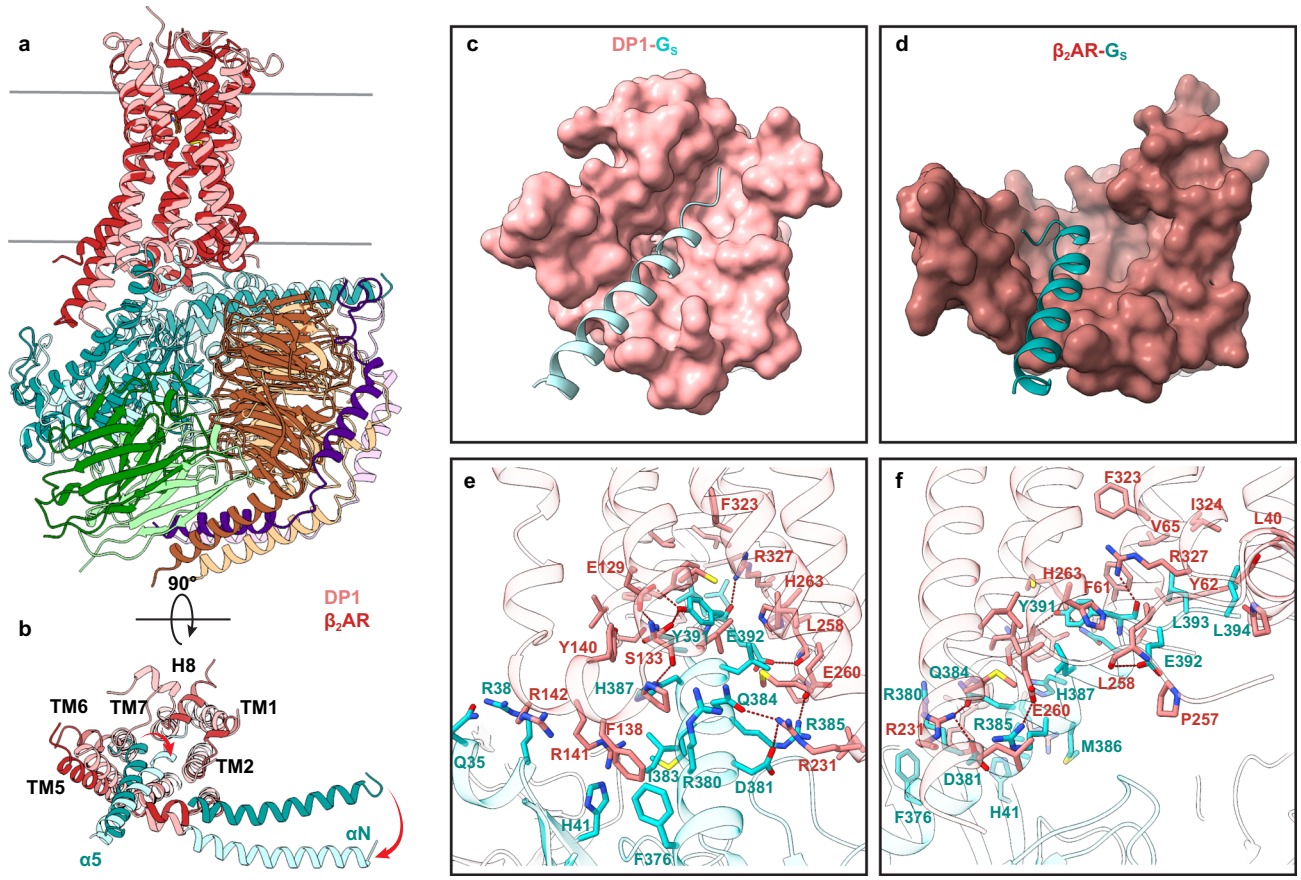

Fig. 5 | DP1-G_s protein binding interface. a, **b** Structural comparison of DP1-G_s complex (light colors) with β_2AR-G_s (3SN6, dark colors), viewed within the lipid membrane (**a**) and from the intracellular side (**b**). In the intracellular view (**b**), most of G_s protein is hidden, with only α5 and αN helices of $G\alpha_s$ helices shown to demonstrate an ~15° clockwise rotation of G_s in DP1 compared to β_2AR. **c**, **d** A more narrow intracellular cavity and a different orientation of the α5 helix in DP1 (**c**) compared to β_2AR (**d**). **e**, **f** Details of the DP1-G_s protein interface shown in two different orientations. Salt bridges and hydrogen bonds are shown as red dashed lines. The following colors are used in this figure: receptor (salmon), $G\alpha_s$ (cyan), Gβ (brown), Gγ (violet), Nb-35 (green).

C379$^{G.H5.11}$, F376$^{G.H5.08}$, V217$^{G.S3.01}$, F219$^{G.S3.03}$, and H41$^{G.S1.02}$ in $G\alpha_s$ (Fig. 5e). The stabilization of the α5 helix is further reinforced by R231$^{5.68}$ and E260$^{6.30}$, which form salt bridges or hydrogen bonds with D381$^{G.H5.13}$/Q384$^{G.H5.14}$ and R385$^{G.H5.17}$, respectively. Despite their involvement in polar interactions with $G\alpha_s$ residues, single mutations of E129$^{3.49}$A and E260$^{6.30}$A showed little effect on the potency of PGD2 (Fig. 4h and Supplementary Table 2), possibly because these interactions could be substituted by other residues. For example, in the case of the E260$^{6.30}$A mutation, the neighboring residue E259$^{6.29}$ may potentially engage in a salt bridge with R385$^{G.H5.17}$.

Distinct conformation of H8

Both the inactive and active states of DP1 display distinctive arrangements of H8, oriented along the membrane and interacting with TM6, unlike the typical H8 conformation contacting TM1 as found in most GPCRs (Fig. 6a, b). In the inactive state, the EM density in this region is sufficient to model the majority of the H8 side chains up to the residue P342$^{8.62}$. However, in the active state structures, the density becomes substantially weaker, allowing only 7 residues to be modeled in the alpha helical conformation followed by 3 unstructured residues, likely due to increased mobility of H8. Overall, the conformation of H8 is maintained through a combination of amphiphilic interactions with the membrane and salt bridges with TM residues. Our MD simulations of the inactive state DP1 support the integrity of H8 and its proximity to TM6 throughout the simulation time of 1.2 μs, showing a stable distance between the Cα atoms of key residues, such as D262$^{6.32}$ in TM6 and R332$^{8.52}$ and R327$^{8.47}$ (Supplementary Fig. 20a, b). The stability of these interactions is further supported by the strong salt bridges observed in MD between the carboxylate group of D262$^{6.32}$ and the guanidinium groups of R332$^{8.52}$ and R327$^{8.47}$ (Supplementary Fig. 20d, e, g, h, j, k). The modeling and analysis of H8 in MD simulations of the active state suggest that the contact between TM6 and H8 is maintained despite the shifts of TM6 and TM7. However, the contact is stabilized by a different salt bridge between D262$^{6.32}$ in TM6 and K337$^{8.57}$ in H8 (Supplementary Fig. 21c, f, i, l), the switch that is likely correlated with the outward shift of TM6 and the corresponding rearrangements in the intracellular region.

Our comparative analysis suggests a distinct role of H8 in DP1 and other prostanoid receptors that differentiates them from other class A receptors. In most class A GPCRs, the classical orientation of H8 along the membrane boundary pointing towards TM1 is stabilized by the conserved side chains of F$^{8.50}$ and F$^{8.54}$ inserted between TM7 and TM1[70] (Fig. 6e). Instead, in DP1 specifically, although this motif is retained, it is shifted by a sequence insertion of an additional residue R327$^{8.47}$, conserved in prostanoid receptors, which in the inactive DP1 structures positions its bulky side chain in the same space between TM7 and TM1 (Fig. 6c). All other prostanoid receptors lack the "FxxxF" motif entirely, with residues in these positions unable to stabilize H8 in its canonical orientation. Indeed, when H8 was resolved in EP2, EP3, EP4 and TP, it was found in contact with TM6 as observed in DP1; although in the active states of EP4, FP and IP, no contacts of H8 with TM6 was observed (Fig. 6d and Supplementary Table 4). Analysis of other prostanoid receptors, combined with our MD simulations of DP1 structures, suggests that the orientation of H8 can be stabilized by

https://doi.org/10.1038/s41467-025-64002-z

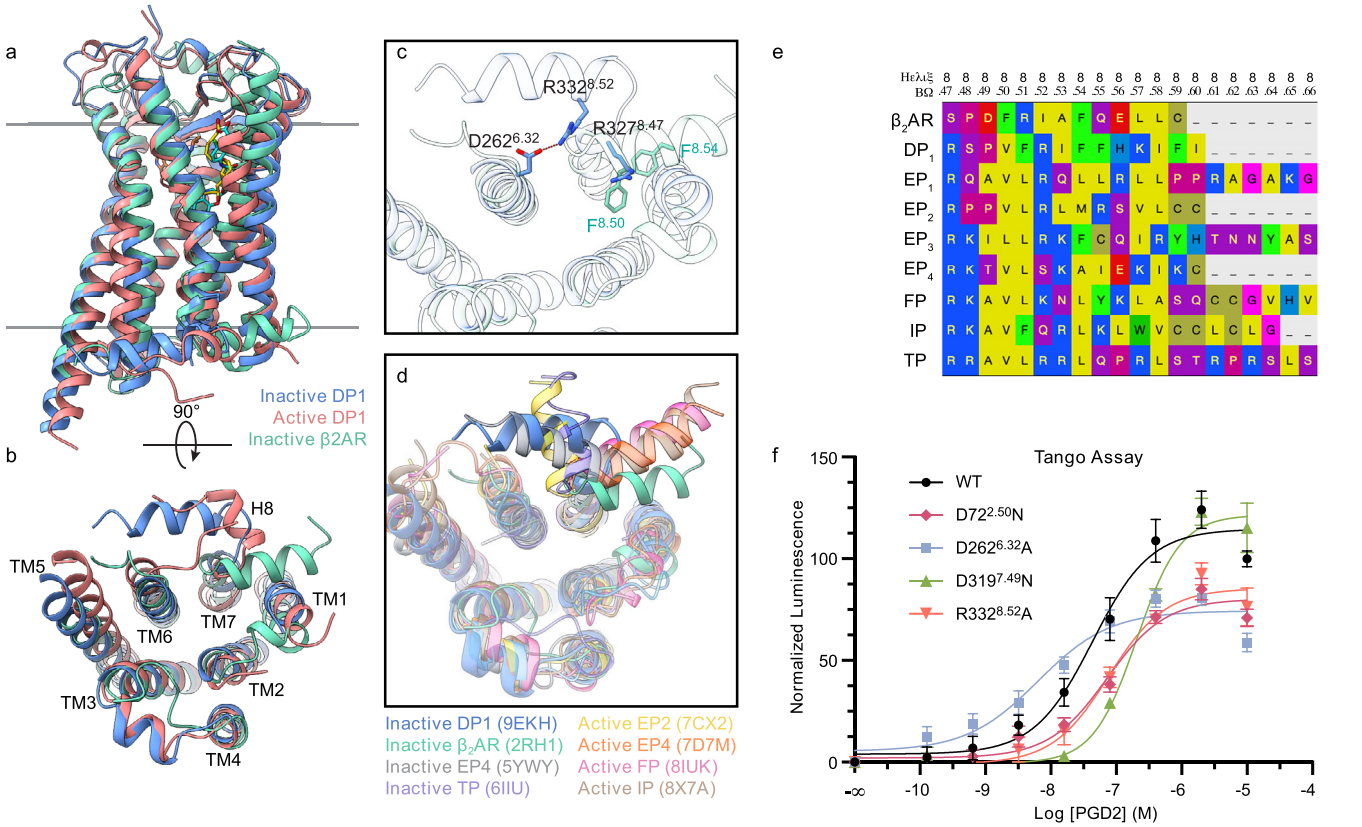

Fig. 6 | Conformation of H8. a, **b** Structural comparison of the inactive (blue) and active (salmon) states of DP1 with the inactive state of β_2AR (aquamarine), viewed within the lipid membrane (**a**) and from the intracellular side (**b**). H8 flips over by almost 180° within the plane of the membrane in DP1 contacting TM6, compared to the classical orientation of H8 in β_2AR contacting TM1. **c** Salt bridge between R332$^{8.52}$ and D262$^{6.32}$ in DP1, and two residues from the classical F$^{8.50}$xxxF$^{8.54}$ motif in β_2AR overlapping with the side chain of R327$^{8.47}$ in DP1. **d** Structural comparison between prostanoid receptors showing orientations of their H8: inactive DP1 (blue, PDB: 9EKH), inactive β_2AR (aquamarine, PDB: 2RH1), inactive EP4 (gray, PDB: 5YWY), inactive TP (violet, PDB: 6IIU), active EP2 (yellow, PDB: 7CX2), active EP4 (orange, PDB: 7D7M), active FP (pink, PDB: 8IUK), active IP (tan, PDB: 8X7A). **e** Multiple sequence alignment of H8 comparing β_2AR with prostanoid receptors. **f** β-arrestin2 recruitment Tango assay showing the concentration-response signal for WT DP1 and several mutants involved in receptor activation and stabilization of H8. The signal is normalized to represent the percent increase above basal. Data points correspond to means ± SEM for three biologically independent experiments conducted in triplicates. The corresponding E_{max} and EC_{50} values are shown in Supplementary Table 5. Source Data are provided as a Source data file.

the salt bridges between the conserved side chains of D/E$^{6.32}$ and R$^{8.52}$ residues, and potentially R$^{8.47}$.

Our DP1 cell signaling assays suggest functional relevance of H8 in both G protein activation and β-arrestin recruitment. The R327$^{8.47}$A mutation almost eliminated PGD2-induced signaling, while decreasing receptor expression by about two times (Fig. 4h, Supplementary Fig. 4a, and Supplementary Table 2). On the other hand, the D262$^{6.32}$A mutation increased the potency of PGD2 in β-arrestin2 recruitment Tango assay[71], whereas R332$^{8.52}$A decreased the potency of PGD2 in both ONE-GO and Tango assays (Figs. 4h and 6f, Supplementary Tables 2 and 5). Additionally, R327$^{8.47}$A and R332$^{8.52}$A decreased DP1 basal signaling in cAMP accumulation assays (Supplementary Fig. 4b). In the active state DP1 structures, R327$^{8.47}$ makes a hydrogen bond with the backbone carbonyl of Y391$^{G.H5.23}$ on the α5 helix of Gα$_s$, while R332$^{8.52}$ also extends toward the α5 helix of Gα$_s$ and may engage in direct or water-mediated interactions with the C-terminal carboxylate of Gα$_s$ or the sidechain of E392$^{G.H5.24}$.

Discussion

Prostanoids represent a diverse group of bioactive lipids derived from arachidonic acid, which includes prostaglandins (PGD2, PGE2, PGF2α), prostacyclins (PGI2), and thromboxanes (TXA2)[72]. They exert their action by activating specific prostanoid G protein-coupled receptors, regulating various physiological and pathological processes such as inflammation, vascular tone, platelet aggregation, gastrointestinal protection, and reproductive functions. Structures of seven out of the nine prostanoid receptors in at least one of their conformational states have been published[37–51], except for DP1 and EP1 receptors. Elucidating these missing structures is essential to fully unravel the molecular basis of prostanoid signaling and to support the rational design of receptor-specific therapeutics targeting these critical signaling pathways.

In this study, we report five high-resolution cryo-EM structures of DP1 captured in distinct functional states, including the apo state, the inactive state bound to two inverse agonists, developed by ONO Pharmaceutical, and the active G$_s$ protein-coupled state bound to PGD2 and BW245C. The DP1 receptor responds to elevated extracellular concentrations of PGD2, predominantly released by immune cells. Upon activation, DP1 transmits the signal inside the cell by coupling to G$_s$ proteins, leading to an increase in intracellular cAMP levels. This elevation in cAMP initiates downstream signaling cascades that modulate key physiological processes, including the regulation of inflammation, immune responses, and smooth muscle relaxation. Through an integrated approach combining structural analysis, site-directed mutagenesis coupled to functional assays, and MD simulations, we elucidated the molecular determinants of ligand recognition and selectivity, as well as the mechanisms underlying DP1 receptor activation and inhibition. Furthermore, comparative analyses with other structurally characterized prostanoid receptors revealed both conserved and distinct structural motifs that govern ligand recognition, receptor activation, and G protein coupling efficiency.

Similar to other prostanoid receptors, the ligand binding pocket of the inactive DP1 receptor is capped on the extracellular side by the ECL2 and N-terminus, stabilized by two disulfide bonds. The pocket, however, remains open towards the lipid membrane via a gap between TM1 and TM7, through which lipid-like ligands likely enter and exit the binding site. Agonist binding induces shifts in TM1 and TM7, resulting in an almost fully occluded binding pocket. The recognition of endogenous ligands occurs mainly through conserved in prostanoid receptors residues $Y^{2.65}$, T/S^{ECL2}, and $R^{7.40}$ that engage in hydrogen bond and salt bridge interactions with the carboxylic group of the ligand, as well as through hydrophobic interactions with conserved residues W^{ECL2}, $M/L^{3.32}$, and $L/F^{7.36}$. The selectivity towards specific prostanoids is achieved through specific interactions with the central ring. In DP1, the central D-ring of PGD2 makes a polar interaction with $S80^{2.58}$, conserved in EP2, EP4 and IP, and a hydrogen bond with non-conserved $K76^{2.54}$.

The DP1 receptor lacks most of the conserved motifs of class A GPCRs, resulting in a distinct activation mechanism, the key role in which is played by residue $K76^{2.54}$ not found in any other receptor. In the inactive state, the $K76^{2.54}$ side chain substitutes for the sodium ion by occupying the sodium binding pocket and forming a salt bridge with the conserved $D72^{2.50}$. Upon agonist binding, $K76^{2.54}$ switches its conformation to form hydrogen bonds with the ligand, allowing the sodium binding pocket to collapse and the activation-related conformational changes to propagate toward the intracellular side of the receptor. The hydrophobic bulky meta-xylene ring of the inverse agonists restricts the conformational flexibility of $K76^{2.54}$, favoring its interaction with $D72^{2.50}$ and thereby stabilizing the inactive state. Thus, $K76^{2.54}$ serves as a critical molecular switch between the inactive and active states in DP1.

Additionally, DP1 exhibits a distinct conformation of H8 in both inactive and active states, oriented toward TM6 rather than the classical orientation of H8 toward TM1 observed in other class A GPCRs. This H8 arrangement is influenced and stabilized by the insertion of the $R^{8.47}$ residue, conserved in prostanoid receptors, which can make salt bridges with TM6—a feature shared with several other prostanoid receptors. This distinct configuration of H8 appears to play functionally important role in modulating both G protein and β-arrestin signaling.

The activation-associated displacement of the intracellular part of TM6 in DP1 is substantially smaller compared to other G_s-coupled receptors, resulting in a narrower intracellular cavity on the intracellular side of the receptor. This leads to rotation of the heterotrimeric G_s protein to insert its α5 helix at a different angle and extending its C-terminus toward TM1 rather than TM6 as in most other class A receptors. This distinct G_s protein binding interface is also observed in other G_s-coupled prostanoid receptors such as EP2, EP4, and IP.

In conclusion, although DP1 shares certain conserved sequence motifs, ligand recognition features, and G protein coupling arrangements with other prostanoid receptors, it exhibits several distinctive structural characteristics that define its specific mechanisms of activation and inhibition. These features offer valuable insights that could be further leveraged for the rational development of therapeutics selectively targeting DP1.

Methods

DP1 construct design for cryo-EM structure determination

For DP1 active state structure determination, the *PTGDR* gene (UniProt Q13258) encoding the human wild type (WT) DP1 receptor was codon-optimized for primary expression in insect cells and synthesized by GenScript. The construct includes an N-terminal hemagglutinin (HA) signal peptide (KTIIALSYIFCLVFA) to facilitate cell surface delivery and a Flag-tag epitope (DYKDDDD) for assessing surface expression. At the C-terminus, the construct features an HRV-3C protease cleavage site, followed by a flexible linker (GSGGGGSGGGG), enhanced green fluorescent protein (eGFP), and an 8×His tag for rapid screening of the expression system and purification purposes.

For the inactive state $DP1_{ICL3}$bRIL construct, the human WT *PTGDR* gene was similarly codon-optimized and synthesized by GenScript, including the HA signal peptide and FLAG tag at the N-terminus, identical to the active construct. The bRIL fusion was inserted into ICL3, replacing residues R234-P257 and inserting a short linker (ERARSTL) at the TM6 side of the junction. The receptor sequence was followed by an HRV3C protease cleavage site and an 8×His tag at the C-terminus. Three point-mutations $C130^{3.50}R$, $H263^{6.33}A$, and $D319^{7.49}N$ were introduced using oligonucleotides (IDT) with internal mismatches and AccuPrime Pfx polymerase (Thermo Fisher Scientific) and verified by Sanger sequencing (Genewiz). The modified DP1 plasmids were subcloned into pFastBac vectors (Invitrogen) for baculovirus expression in insect cells.

Expression and purification of an anti-bRIL Fab (BAG2)

The anti-bRIL Fab (BAG2) plasmid[56] (a gift from Dr. Kossiakoff), was expressed and purified according to published protocols[56–58]. Briefly, BAG2 Fab in the pRH2.2 vector was transformed into *E. coli* BL21 Rosetta cells, cultured overnight in Miller's Luria Broth (LB) media with carbenicillin at 225 rpm and 37 °C. The culture was used to inoculate 1 L of 2× Yeast Extract Tryptone (YT) media with glucose, $MgCl_2$, and carbenicillin, and grown until an OD600 of 0.6–0.8. Fab expression was induced with 1.0 mM IPTG, and the culture was incubated at 20 °C for 21 h. Cells were harvested, lysed in a lysing buffer containing 20 mM HEPES pH 7.5, 150 mM NaCl, DNaseI, and homemade protease inhibitor (PI) cocktail, and sonicated three times using a Q500 sonicator (Qsonica) with a standard probe 4220 and the following settings: Amp 95%, pulse on: 5 s, pulse off: 10 s, for a total of 3 min. The lysate was heated to 60–63 °C for 30 min to improve the purity of Fab by removing unstable bacterial proteins and Fab degradation products. The lysate mixture was further centrifuged, and the supernatant was purified using a HiTrap Protein L column (5 mL). The Fab was eluted, concentrated to 15 mg/mL using 30-kDa cutoff Amicon Ultra Centrifugal Filter (Millipore). The final buffer is exchanged to 20 mM HEPES pH 7.5, 150 mM NaCl, 20% glycerol, and flash-frozen for storage at −80 °C.

Expression and purification of an anti-Fab nanobody (Nb)

The anti-Fab nanobody (Nb) was also prepared as previously described[58]. The Nb vector was introduced into BL21 *E. coli* cells, which were cultured overnight in LB media with kanamycin at 37 °C. The next day, this culture was used to inoculate 1 L of Terrific Broth (TB) media supplemented with kanamycin and grown until the OD600 reached 0.6–0.8. The cells were then induced with 1.0 mM IPTG and incubated for an additional 18–20 h at 30 °C. After induction and incubation, the cells were harvested by centrifugation and stored at −80 °C. The cell pellet was resuspended in cold Tris-EDTA-Sucrose (TES) buffer containing 50 mM Tris pH 8.0, 0.5 mM EDTA, and 20% sucrose, then stirred for 1 h at 4 °C. An additional 40 mL TES was added and stirred for another hour at 4 °C, followed by centrifugation at 10,000 × *g* for 30 min. The resulting supernatant constituted the periplasmic extract, and the His-tagged Nb was purified using a Ni-NTA resin, eluted with 250 mM imidazole, and further purified via Superdex 200 10/300 GL. The purified Nb was concentrated to 10 mg/mL using a 10-kDa cutoff Amicon Ultra Centrifugal Filter (Millipore). The final buffer is exchanged to 20 mM HEPES pH 7.5, 150 mM NaCl, 20% glycerol, and flash-frozen for storage at −80 °C.

Expression and purification of Nb35

The Nb35 plasmid[64] was introduced into BL21 *E. coli* cells and cultured overnight in LB media supplemented with 2% glucose, 1 mM $MgCl_2$, and carbenicillin at 37 °C in a shaking incubator at 225 rpm. The

following day, this culture was used to inoculate 1 L of TB media supplemented with 0.1% glucose, 1 mM $MgCl_2$, and carbenicillin. The cells were grown until they reached an OD600 of 0.6–0.8, then induced with 1.0 mM IPTG. After induction, the temperature was reduced to 20 °C, and the cells were incubated for an additional 22 h. The cells were then harvested by centrifugation and stored at −80 °C. Nb35, which is expressed in the periplasmic space, was purified using nickel affinity chromatography followed by size exclusion chromatography, concentrated to 10 mg/mL, using a 10-kDa cutoff Amicon Ultra Centrifugal Filter (Millipore). The final buffer was exchanged to 20 mM HEPES pH 7.5, 150 mM NaCl, 20% glycerol, and flash-frozen in aliquots, stored at −80 °C for future use.

Expression and purification of $DP1_{ICL3}$bRIL-BAG2-Nb complex

The $DP1_{ICL3}$bRIL construct was expressed in *Spodoptera frugiperda (*Sf9*)* insect cells (Expression Systems, Cat# 94-001F) using the Bac-to-Bac baculovirus expression system (Invitrogen). Cells were infected at a density of ~2×10^6 cells/mL at MOI of 5 and grown for 48 h at 37 °C. Cells were harvested by centrifugation and stored at −80 °C. The frozen cell pellets were initially thawed and lysed in a hypotonic buffer (10 mM HEPES pH 7.5, 10 mM $MgCl_2$, and 20 mM KCl) using dounce homogenizer, followed by centrifugation. The lysed cells were further washed two times using high osmotic buffer (10 mM HEPES pH 7.5, 1.0 M NaCl, 10 mM $MgCl_2$, and 20 mM KCl) supplemented by homemade protease inhibitor (PI) cocktail (containing AEBSF, E-64, leupeptin, and aprotinin), thus separating soluble and membrane associated proteins from integral transmembrane proteins. Washed membranes were re-suspended and homogenized by douncing in a buffer containing 2 mg/mL iodoacetamide, 20 μM (S)-1-(2-chloro-5-(2,6-dimethyl-4-((4-methyl-3,4-dihydro-2H-benzo[b][1,4]oxazin-2-yl)methoxy)benzamido)phenyl)cyclopropane-1-carboxylic acid (ONO3030297) or (S)-2-(2-chloro-5-(2,6-dimethyl-4-((4-methyl-3,4-dihydro-2H-benzo[b][1,4]oxazin-2-yl)methoxy)benzamido)phenyl)acetic acid (ONO2550289) (a gift from ONO Pharmaceutical)[73], and PI cocktail and incubated at 4 °C for 30 min. The membranes were then solubilized in a buffer containing 25 mM HEPES pH 7.5, 500 mM NaCl, 0.5% (w/v) lauryl maltose neopentyl glycol (LMNG, Anatrace) and 0.05% (w/v) cholesteryl hemisuccinate (CHS, Sigma-Aldrich) for 2 h at 4 °C. Insoluble debris was removed with ultracentrifugation at 60,000 × *g* for 50 min, and solubilized receptor was incubated with 20 mM imidazole and Talon (immobilized metal affinity chromatography IMAC) resin (Clontech) overnight at 4 °C. The following day, the receptor-bound resin was collected in a column and washed extensively with twenty column volume wash buffer-1 (25 mM HEPES pH 7.5, 800 mM NaCl, 20 μM ONO compound, 0.1% (w/v) LMNG, 0.01% (w/v) CHS, and 20 mM imidazole) and ten column volume wash buffer-2 (25 mM HEPES pH 7.5, 150 mM NaCl, 20 μM ONO compound, 0.05% (w/v) LMNG, 0.005% (w/v) CHS, and 30 mM imidazole). The $DP1_{ICL3}$bRIL protein was then eluted using elution buffer (25 mM HEPES pH 7.5, 150 mM NaCl, 20 μM ONO compound, 0.02% (w/v) LMNG, 0.002% (w/v) CHS, and 250 mM imidazole).

To prepare the $DP1_{ICL3}$bRIL-BAG2-Nb complex, the purified ligand-bound $DP1_{ICL3}$bRIL was then incubated overnight at 4 °C with a 1.5-fold molar excess of BAG2 (anti-bRIL Fab) and a 2-fold molar excess of Nb (Fab-stabilizing nanobody). The following day, the mixture was injected into a Superdex 200 10/300 GL column, equilibrated with running buffer (20 mM HEPES pH 7.5, 100 mM NaCl, 0.00075% (w/v) LMNG, 0.000075% (w/v) CHS, 0.00025% (w/v) GDN, and 20 μM ONO compound). Fractions corresponding to the peak of the complex were collected and concentrated using a 100-kDa cutoff Amicon Ultra Centrifugal Filter (Millipore) for cryo-EM analysis.

Expression and purification of the human DP1-G_s-Nb35 complex

Human DP1, DNGα_s, and G$\beta_1\gamma_2$ were co-expressed in Sf9 insect cells using the Bac-to-Bac baculovirus expression system (Invitrogen). Cell cultures were grown to a density of ~2×10^6 cells/mL in ESF 921 serum-free medium (Expression Systems). Subsequently, the Sf9 cells were co-infected by three baculoviruses encoding DP1, DNGαs, and G$\beta_1\gamma_2$ at a multiplicity of infection (MOI) of 5 at a 1:1:1 ratio. The cells were harvested by centrifugation 48 h after infection, and cell pellets were stored at −80 °C until further use. Frozen cell pellets were thawed in a hypotonic buffer containing 20 mM HEPES pH 7.5, 100 mM NaCl, 5 mM $MgCl_2$, and 5 mM $CaCl_2$, 0.1 mM TCEP supplemented with homemade PI cocktail. After homogenization, 25 mU/mL apyrase (New England Biolabs), 200 μM PGD2 or 20 μM BW245C, and 10 μg/mL Nb35 were added to the suspension and incubated at room temperature for 1 h. Membranes were collected by ultracentrifugation for 30 min and further solubilized with 20 mM HEPES (pH 7.5), 100 mM NaCl, 5 mM $MgCl_2$, 5 mM $CaCl_2$, 0.1 mM TCEP, 25 mU/mL apyrase, 0.5% (w/v) LMNG, and 0.05% (w/v) CHS for 2 h at 4 °C. The supernatant was isolated by centrifugation at 30,000 × *g* (Ti45, Beckman) for 45 min. The isolated supernatant was incubated with anti-GFP resin (made in-house) at 4 °C overnight. The resin was washed extensively with three washing steps in buffer containing 20 mM HEPES (pH 7.5), 100 mM NaCl, 0.1 mM TCEP, and 200 μM PGD2 or 20 μM BW245C, supplemented with different concentration of detergents: 0.1% (w/v) LMNG, 0.01% (w/v) CHS in the first wash, 0.05% (w/v) LMNG, 0.005% (w/v) CHS in the second wash. The complex was eluted by incubating with 15–20 IU of HRV-3C protease (GenScript) overnight at 4 °C and further purified on a Superdex 200 10/300 GL column (GE Healthcare) in a running buffer (20 mM HEPES pH 7.5, 100 mM NaCl, 0.00075% (w/v) LMNG, 0.000075% (w/v) CHS, 0.00025% (w/v) GDN, 100 μM TCEP, and 200 μM PGD2 or 20 μM BW245C). The peak fractions of the complex bound to PGD2 and BW245C were collected and concentrated using a 100-kDa cut-off concentrator (Amicon) to approximately 4.2 mg/mL and 7.5 mg/mL for cryo-EM sample preparation, respectively.

Cryo-EM grid preparation

The purified $DP1_{ICL3}$bRIL-BAG2-Nb and DP1-G_s-Nb35 samples (3.0 μL) at a concentration of 4–7 mg/mL were applied to holey carbon grids (Quantifoil R1.2/1.3, 200 mesh), pre-treated by glow-discharging at 20 mA for 40 s. The grids for the $DP1_{ICL3}$bRIL-BAG2-Nb complexes were then blotted for 3.0 s with a 10 s wait time, while the grids for the DP1-G_s-Nb35 complexes were blotted for 2.5–3.5 s with a 5 s wait time, before being vitrified in liquid ethane using a Vitrobot Mark IV (Thermo Fisher Scientific).

Cryo-EM data acquisition and image processing

A total of 7240, 5747, and 5927 movies were collected for the three $DP1_{ICL3}$bRIL-BAG2-Nb complexes in apo form, bound to ONO3030297, and bound to ONO2550289, respectively, using a Titan Krios (Thermo Fisher Scientific) at the Stanford-SLAC Cryo-EM Center (S2C2). The data were acquired with a 300 kV transmission cryogenic electron microscope equipped with a Gatan BioQuantum K3 Energy Filter and a Gatan K3 direct-electron detector. The movies from the $DP1_{ICL3}$bRIL-BAG2-Nb in apo form and bound to ONO3030297 were recorded in super-resolution mode at a magnified physical pixel size of 0.86 Å, with defocus values ranging from −1.2 to −2.0 μm. The total exposure time was 3.1 s, resulting in a total dose of 65 e-/Å^2 (70 frames). For the $DP1_{ICL3}$bRIL-BAG2-Nb complex bound to ONO2550289, the movies were recorded in counting mode at a pixel size of 0.86 Å, with defocus values ranging from −0.8 to −2.2 μm and a total exposure time of 2.33 s at a dose of 65 e-/Å^2 (70 frames).

All datasets were motion-corrected using MotionCor2[74], and the contrast transfer function (CTF) parameters were estimated with Patch CTF in cryoSPARC (v4.5.3 or v4.7.0)[75]. Images with a CTF fit resolution better than 5 Å were selected for further processing. Initially, template-

free particle picking was performed using blob-picker, based on the particles' estimated size range of 80–220 Å. This was followed by 2D classification to create templates for template-based autopicking. Particles were then extracted and subjected to multiple rounds of 2D classification, resulting in the selection of 2,602,357, 690,071, and 969,860 particles for the $DP1_{ICL3}$bRIL-BAG2-Nb complex in apo form, bound to ONO3030297, and bound to ONO2550289, respectively. For ONO3030297, Topaz Train job[76] was further performed using the selected 2D class particles as a template. The resulting particles were consolidated with previously selected particles in 2D classification, and duplicates were removed. The selected particles for all datasets were used to generate ab initio 3D models, followed by 3× iterative heterogenous refinements to clean up junk particles. The best class particles were re-extracted with the box size of 336 pixels for apo and ONO2550289-bound, or 360 pixels for ONO3030297-bound dataset. Ultimately, 530,340, 252,569, and 425,371 particles were subjected to 3D non-uniform refinement, resulting in gold-standard Fourier shell correlation (GSFSC) resolutions of 2.84 Å, 2.87 Å, and 2.91 Å for the $DP1_{ICL3}$bRIL-BAG2-Nb complex in apo form, bound to ONO3030297, and bound to ONO2550289, respectively. For ONO3030297 and ONO2550289-bound datasets, local refinements were further performed with masks focused on the receptor or on the BAG2-Nb, resulting in substantial improvement in map quality compared to the consensus maps. The final composite maps were produced by Combine Focused Maps in Phenix (v.1.21)[77] at the overall nominal GSFSC resolution of 2.89 Å for both maps.

For the DP1-G_s-Nb35 complex bound to PGD2 and BW245C, a total of 10,096 and 9476 movie stacks were acquired, respectively, on a Titan Krios (Thermo Fisher Scientific) at the Core Center of Excellence in Nano Imaging (CNI) of the University of Southern California. The microscope was equipped with a Gatan BioQuantum K3 Imaging Filter and a Gatan K3 direct-electron detector and operated at an acceleration voltage of 300 kV. Images were recorded in super-resolution mode at a defocus range of −0.8 µm to −2.0 µm with a nominal magnification of 105,000×, resulting in a pixel size of 0.84 Å. Each image was dose-fractionated into 50 movie frames with a total exposure time of 3.39 s, resulting in a total dose of 65 $e^-/Å^2$.

All raw movies were corrected for drift and beam-induced motion using MotionCor2[74], and the CTF parameters were estimated using patch CTF estimation in cryoSPARC (v4.7.0)[75]. The initial autopicking process was performed the same way as described above. Multiple rounds of 2D classification and Topaz picking[76] resulted in 1,199,532 and 2,440,146 particles for the DP1-G_s-Nb35 complex bound to PGD2 and BW245C, respectively, after removing duplicate particles. The selected particles were then used for ab initio 3D reconstruction, followed by 5× or 4× iterative heterogenous refinements, and the clean particle stacks were re-extracted with a box size of 360 pixels. Subsequently, a total of 363,286 and 1,072,665 particles underwent 3D non-uniform refinement, yielding GSFSC resolutions of 2.67 Å and 2.47 Å for the DP1-G_s-Nb35 complex bound to PGD2 and BW245C, respectively. Local refinements with masks focused on the receptor or on the heterotrimeric G_s protein-Nb35 complex further improved the map quality. The final composite map was generated by Combine Focused Maps in Phenix (v.1.21)[77] at GSFSC resolutions of 2.68 Å and 2.45 Å for the DP1-G_s-Nb35 complex bound to PGD2 and BW245C, respectively. All maps were sharpened by Sharpening Tool in cryoSPARC (v.4.7.0)[75].

Model building and refinement

For building an atomic model of the $DP1_{ICL3}$bRIL-BAG2-Nb complex, an AlphaFold2[78] model for $DP1_{ICL3}$bRIL and the PDB entry 6WW2[57] for BAG2-Nb were used as the initial model templates. For the DP1-G_s-Nb35 complex, an AlphaFold2[78] DP1 model and the PDB entry 7CX2[37] were used as initial model templates for fitting in experimental density maps using UCSF ChimeraX[79]. The generated structures were manually inspected and adjusted in Coot (v.0.9.8.93)[80] and further refined using *phenix.real_space_refine* within Phenix (v.1.21)[77]. The ligands were then added and manually fitted in Coot. The overall model was further refined and validated by Phenix.

DP1 construct design and site directed mutagenesis for functional assays

Both WT DP1 and $DP1_{ICL3}$bRIL constructs previously used for insect cell expression were subcloned into a pcDNA™3.1(-) vector (Thermo Fisher Scientific, Cat# V79520). Using structure-based analysis and molecular dynamic simulations, 23 mutations deemed important for DP1 function were identified and introduced separately to the WT DP1 construct using Agilent QuickChange site-directed mutagenesis with synthetic primers (Integrated DNA Technologies), AccuPrime™ Pfx SuperMix (Invitrogen, Cat# 12344-040) and DpnI restriction enzyme (New England Biolabs, Cat# R0176S) in rCutsmart buffer (New England Biolabs, Cat# B6004S). For cAMP assay, the GloSensor™ Technology -22F cAMP Plasmid (Promega, Cat# E2301) was purchased from Promega. For ONE-GO assay[54], the ONE-GO Biosensors Kit was a gift from Mikel Garcia-Marcos (Addgene kit #1000000224). For TANGO assay[71], the *PTGDR*-TANGO plasmid was a gift from Bryan Roth (Addgene plasmid # 66482). Five mutations, deemed to be important for β-arrestin recruitment ($D72^{2.50}N$, $D262^{6.32}A$ $D319^{7.49}N$, $R332^{8.52}A$), were introduced to the TANGO plasmid in a similar manner described above. The sequences for all plasmids were sequence verified using the Genewiz (Azenta) sanger sequencing service.

Cell culture for functional assays

Both Human Embryonic Kidney 293T (HEK293T) cells (ATCC, Cat# CRL-3216) and HTLA cells[81] (a gift from Dr. Majumdar) were maintained in culture flasks using Complete Dulbecco's modified Eagle medium (DMEM) Media (Thermo Fisher Scientific, Cat# 11995065) supplemented with 10% heated inactivated Fetal Bovine Serum (FBS) (Thermo Fisher Scientific, Cat# 10082147), 2 mM L-Glutamine (Thermo Fisher Scientific, Cat# 25030081), 100 U/mL–100 µg/mL penicillin-streptomycin (Thermo Fisher Scientific, Cat# 15140122) and grown in a humidified atmosphere at 37 °C and 10% CO_2. Cells were passed biweekly and seeded at a density of 10,000 cells/cm^2 with respect to the size of the culture flask once every 3–4 d using 0.1% trypsin-EDTA (Thermo Fisher Scientific, Cat# 15400054).

Surface expression measurement by flow cytometry

Prior to conducting functional studies, surface expression levels of each DP1 construct were measured relative to WT DP1 using flow cytometry to detect the presence of a FLAG tag. A FLAG tag labeling solution was prepared by performing a 1:100 dilution on an ANTI-FLAG® M2-FITC antibody commercial stock (~1 mg/mL) (Sigma Aldrich, Cat# F4049) using 1× TBS (Corning, Cat# 46-012-CM) supplemented with 4% Bovine Serum Albumin (BSA) (Sigma Aldrich, Cat# A9576). A FITC + 7-AAD working stock was then prepared by performing a 1:6 dilution of a commercial 50 µg/mL 7-AAD stock (Thermo Fisher Scientific, Cat# 00-6993-59) using the previously prepared Anti-FLAG FITC solution to achieve final concentrations of 8.3 µg/mL for both ANTI-FLAG® M2-FITC and 7-AAD. A second working stock was prepared in the same manner as described above, but was diluted with a 1× TBS, 4% BSA supplemented with 1.5% of Triton™ X-100 solution (Sigma Aldrich, Cat# X100).

HEK293T cells were seeded in a 24-chamber culture dish (Corning, Cat# 3524) at a density of 2.0×10^5 cells per chamber in 1 mL of Complete DMEM Media. 5–7 h after seeding, each chamber was transfected with 200 ng of a given DP1 construct (including empty vector as a negative control) using TransIT®-2020 transfection reagent (Mirus, Cat# MIR 5404) at a 1:3 ratio of DNA(µg):TransIT(µL) in Opti-MEM serum free media (Thermo Fisher Scientific, Cat# 31985062). Transfected cells were allowed to incubate overnight, after which the media was replaced with Assay Media, containing DMEM, high glucose,

HEPES, no phenol red media (Thermo Fisher Scientific, Cat# 21063029) supplemented with 1% dialyzed Fetal Bovine Serum (dFBS) (Thermo Fisher Scientific, Cat# 26400044), 2 mM L-glutamine (Thermo Fisher Scientific, Cat# 25030081), 1 mM sodium pyruvate (Thermo Fisher Scientific, Cat# 11360070), and 100 U/mL penicillin - 100 μg/mL streptomycin (Thermo Fisher Scientific, Cat# 15140122) to avoid potential ligands present in FBS that could lead to unwanted activation and desensitization of our receptor. Cells were then incubated for an additional night to allow for maximal expression.

Transfected cells were removed from their incubator and washed with 1× Dulbecco's Phosphate-Buffered Saline (DPBS) (Quality Biological, Cat#119-068-101), then unadhered using 1× versene (Thermo Fisher Scientific, Cat# 15040066) and transferred to 1.5 mL Eppendorf tubes. The cell mixture was centrifuged at 100 × *g* for 5 min, after which the supernatant was removed, and the cell pellet was resuspended in 50 μL of Assay Media. The resuspended cells were transferred into two separate wells, 10 μL each, of a round bottom 96-well plate (Corning, Cat# 3799). Each well was then individually mixed with 10 μL of either the FITC + 7-AAD or FITC + 7-AAD + Triton X-100 working stock solutions. The plate was incubated for 20 min, after which the cells were diluted with 180 μL of 1× TBS buffer (Corning, Cat# 46-012-CM). The plate was then run through a Millipore Guava EasyCyte™ 6HT-2L flow cytometer controlled by the Millipore guavaSoft - ExpressPlus (v.3.6) software, with the instrument being set to count 10,000 cells (error of <1%) and simultaneously measure respective forward scattering, red fluorescence to detect dead cells (640 nm laser and a Red-B 680/30 nm fluorescent filter) and green fluorescence to measure receptor expression (green 488 nm 20 mW laser and a Green-B 525/30 fluorescence filter). Using WT DP1 and empty vector transfected cells, suitable gating, gain and threshold settings were determined to ensure adequate spread and separation of the data points (Supplementary Fig. 22).

To determine the relative total surface expression of each construct with respect to the WT DP1, the mean green fluorescence signal from live expressing cells of the corresponding construct was normalized by the signal from WT DP1 and expressed in percents.

Cyclic AMP GloSensor assay

HEK293T cells were seeded in a 6-chamber culture dish (Corning, Cat# 3516) at a density of 1.5×10^6 cells per well in 3 mL of Complete DMEM Media. The cells were incubated for 5–7 h at 37 °C in a 10% CO_2 atmosphere, after which a transfection mixture was prepared by diluting a 1.5 μg DNA mixture containing 0.2 μg of receptor DNA and 1.3 μg of GloSensor DNA (-22F, Promega, Cat# E2301) in 145 μL Opti-MEM serum-free media (Thermo Fisher Scientific, Cat# 31985062) and mixed with 4.5 μL of TransIT®-2020 transfection reagent (Mirus, Cat# MIR 5404) (1:3 ratio of DNA(μg):TransIT(μL)). The resulting mixture was incubated for 25 min to facilitate complex formation and distributed dropwise with gentle rocking of the cell containing dish after which the cells were allowed to incubate overnight at 37 °C and 10% CO_2. Following overnight incubation, transfected cells were washed with 1× Dulbecco's Phosphate-Buffered Saline (DPBS) (Quality Biological, Cat# 119-068-101) and transferred to a poly-D-lysine treated (Thermo Fisher Scientific, Cat# A3890401) white bottom 96-well plate (Corning, Cat# 3917) using 1× versene (Thermo Fisher Scientific, Cat# 15040066) at a density of 50,000 cells/well in 100 μL of Assay Media containing DMEM, high glucose, HEPES, no phenol red media (Thermo Fisher Scientific, Cat# 21063029) supplemented with 1% dialyzed Fetal Bovine Serum (dFBS) (Thermo Fisher Scientific, Cat# 26400044), 2 mM L-glutamine (Thermo Fisher Scientific, Cat# 25030081), 1 mM sodium pyruvate (Thermo Fisher Scientific, Cat# 11360070), and 100 U/mL penicillin - 100 μg/mL streptomycin (Thermo Fisher Scientific, Cat# 15140122) and serially diluted and incubated for an additional night at 37 °C in a 10% CO_2 atmosphere. For inverse agonism trials involving ONO2550289 and ONO3030297, cells were transfected with triple the amount of receptor and at a higher DNA to cell ratio to account for the relatively low basal activity of DP1, ensuring the detection of measurable effects induced by the inverse agonists. In line with the methods described above, 1.5×10^6 HEK293T cells were transfected with 0.6 μg of receptor DNA and 1.4 μg of GloSensor DNA for a total of 2.0 μg of DNA using 194 μL of Opti-MEM serum-free media and 6 μL of TransIT-2020 reagent (1:3 ratio of DNA(μg):TransIT(μL)).

The following day, 200 μL of 30 mg/mL GloSensor™ Assay Reagent (Promega, Cat# E1290) dissolved in 10 mM HEPES pH 7.5 was diluted in 10 mL of Assay Media, resulting in a final GloSensor reagent concentration of 0.6 mg/mL. This GloSensor supplemented Assay Media was used to replace the existing cell growth media in the 96-well plate containing transfected cells, with 80 μL added to each well. The plate was then incubated at room temperature in the dark for 100 min, after which a total luminescence pre-read was obtained to measure basal activity. 10 μL of 240 μM 3-isobutyl-1-methylxanthine (IBMX) diluted in Assay Media was then added to each well and incubated for an additional 20 min. 20 mM stock solutions of each ligand including PGD2 (MedChemExpress, Cat# HY-101988), BW245C (Cayman Chemical, Cat# 12050), ONO2550289 and ONO3030297 (Ono Pharmaceutical) were prepared in DMSO (Thermo Fisher Scientific, Cat# D12345). The ligand stocks were diluted to a 400 μM (4× working solution) using Assay Media. The 4× working solutions were then serially diluted across 8 points with Assay Media using a 1:8 dilution factor, resulting in a concentration range from 400 μM to 190.8 pM (final 1× concentrations from 100 μM to 47.7 pM). Next, 30 μL of the 4× serially diluted ligand solutions were added to their respective wells resulting in a final volume of 120 μL at a final ligand concentration of 1×. A total luminescence signal was immediately measured in each well using a BioTek Synergy H4 Hybrid Multi-Mode Microplate reader with a hole filter at 22 °C over 45 min, with 2 min 30 s reading intervals and an integration time of 1 s. The protocol was repeated across 3 biologically independent trials ($n = 3$) with each independent trial consisting of 3 or 24 technical replicas per condition.

Due to the inherent cytotoxicity of PGD2[82], data at 100 μM concentration were omitted from further analysis. For agonists, raw luminescence values collected 30 min after ligand addition were normalized to the maximal signal from 12.5 μM PGD2 at WT DP1 (set at 100%) and the basal signal from wells without added drug (set at 0%). For inverse agonists, the raw data were normalized to the basal signal (set at 0%) and the signal from empty vector-transfected cells (set at −100%). The normalized data were then analyzed using nonlinear regression with the log(agonist) vs. response - variable slope (four parameters) model in GraphPad Prism v. 10.0.2.

β-Arrestin2 recruitment TANGO assay

For measuring β-Arrestin2 recruitment, the TANGO assay[71,81] was used. HTLA cells were seeded in a 6-chamber dish at a density of 1.5×10^6 cells per chamber in Complete DMEM Media. Cells were incubated for 5–7 h at 37 °C in a 10% CO_2 atmosphere, after which cells were transfected with 1.5 μg of a given DP1 construct in a TANGO vector using the same transfection protocol as in the GloSensor assay section. Cells were incubated overnight and then transferred using 1× versene (Thermo Fisher Scientific, Cat# 15040066) to a poly-D-lysine treated (Thermo Fisher Scientific, Cat# A3890401) white bottom 96-well plate (Corning, Cat# 3917) at a density of 50,000 cells/well in 100 μL of Assay Media and incubated for an additional night. The following day, a 20 mM PGD2 (MedChemExpress, Cat# HY-101988) stock in DMSO was diluted to 30 μM (3× solution) using Assay Media containing DMEM, high glucose, HEPES, no phenol red media (Thermo Fisher Scientific, Cat# 21063029) supplemented with 1% dialyzed Fetal Bovine Serum (dFBS) (Thermo Fisher Scientific, Cat# 26400044), 2 mM L-glutamine (Thermo Fisher Scientific, Cat# 25030081), 1 mM sodium pyruvate (Thermo Fisher Scientific, Cat# 11360070), and 100 U/mL penicillin - 100 μg/mL streptomycin (Thermo Fisher Scientific, Cat# 15140122) and

serially diluted and serially diluted over 8 points using a 1:5 dilution factor to achieve a concentration range from 30 μM to 384 pM (final 1× concentrations from 10 μM to 128 pM). 50 μL of serially diluted 3× PGD2 was then added directly to the cell media of each respective well, and the cells were allowed to incubate for an additional night. On day 3, the Assay Media was aspirated and replaced with TANGO Assay Buffer (20 mM HEPES pH 7.4, 1x HBSS) containing 1:20 fold diluted Bright-Glo (Promega) reagent. Luminescence was measured using a BioTek Synergy H4 Hybrid Multi-Mode Microplate plate reader equipped with a hole filter at 22 °C over 45 min with 2 min 30 s reading intervals and integration time of 1 s per well. A total of 3 independent trials ($n = 3$) were conducted, each independent trial consisting of 3 repeats per condition. Wells without added ligand were used to measure basal activity while cells transfected with an empty vector served as a negative control for background luminescence.

The raw luminescence concentration-response data, collected 30 min after Bright-Glo reagent addition, were normalized to reflect the percentage change relative to the basal signal. The normalized data were analyzed using nonlinear regression with the log(agonist) vs. response - variable slope (four parameters) model in GraphPad Prism v. 10.0.2.

ONE-GO BRET G_s protein activation assay

The ONE-GO BRET assay[54,55] measures direct G protein activation by using selective biosensor towards specific Gα subunits. The biosensor comprises a single plasmid encoding specific YFP-fused Gα subunit and membrane-anchored nanoluciferase fused to a peptide or protein domain exhibiting high selectivity binding towards the corresponding Gα-GTP complex. HEK293T cells were seeded in a 6-chamber culture dish (Corning, Cat# 3516) at a density of 350,000 cells per well in 2 mL of Complete DMEM Media and incubated overnight. The following day, cells were transfected with the respective receptor construct in pcDNA3.1 (200 ng), ONE-GO $G\alpha_s$ BRET sensor in pcDNA3.1 (50 ng), and empty vector pcDNA3.1 (750 ng, to facilitate homogeneous distribution of the target DNA) using PEI STAR™ transfection reagent (Tocris, Cat# 7854) at a ratio of 1:3 DNA(μg):PEI(μg). After transfection, the cells were allowed to incubate overnight at 37 °C and 10% CO_2. The following day ONE-GO assay was performed.

PGD2 (MedChemExpress, Cat# HY-101988) was dissolved to 20 mM in DMSO (Thermo Fisher Scientific, Cat# D12345). The stock was then further diluted to 30 μM (3×) using BRET buffer (140 mM NaCl, 5 mM KCl, 1 mM $MgCl_2$, 1 mM $CaCl_2$, 0.37 mM NaH_2PO_4, 20 mM HEPES pH 7.4, 0.1% Glucose). The 30 μM working stocks were then serially diluted using a 1:8 dilution factor across 7 points to produce 3× stocks with a concentration range from 30 μM to 114 pM with the final 8th point containing no drug as a control. Once prepared, the 6-chamber culture dish containing the transfected cells were removed from the incubator, media was aspirated from each chamber and the cells were unadhered via trituration using 1 mL of DMEM, high glucose, HEPES, no phenol red media (Thermo Fisher Scientific, Cat# 21063029). Unadhered cells were transferred to an Eppendorf tube and centrifuged at 500 × g for 5 min. The supernatant was aspirated, and the pelleted cells were resuspended in 300 μL of BRET Buffer to produce a cell density of ~1.5×10^6 cells/mL. 10 μL of resuspended cells were then transferred to each well (15,000 cells/well) of a white bottom 384-well plate (Revvity, Cat# 6007290), and centrifuged at 200 × g for 2 min. 10 μL of 3× serially diluted drug was then added to respective wells after which the cells were centrifuged once more at 200 × g for 2 min and incubated for 5 min to allow for drug binding. During the incubation, 30 μM (3×) Coelenterazine 400a (CTZ400a, Nanolight Technology, Cat# 340-10) solution was prepared by diluting 2 mM CTZ400a stock in NanoFuel-400a solvent (Nanolight Technology, Cat# 397-10) using BRET buffer. After a 5-min incubation, 10 μL of the 3× CTZ400a solution was then distributed across all wells, and the plate was centrifuged at 200 × g for 2 min. The plate was then inserted into a PHERAstar FSX plate reader (BMG Labtech), and a gain adjustment was performed using the well with the highest expected luminescence. Using the adjusted gain, a kinetic reading was recorded over 30 min at 28 °C using a top optic BRET 1 plus optic module (535-30 nm and 475-30 nm filters) with simultaneous dual emission detection and 0.32 s measurement intervals. The protocol was repeated across 3 biologically independent trials ($n = 3$) with each independent trial consisting of 3 technical replicas per condition.

The emission data were observed to stabilize after 6 min post CTZ400a addition, and these time points were used for further data processing. BRET ratios were calculated by dividing the 535-30 nm emission by the 475-30 nm emission in the PHERAstar FS MARS (v. 5.02 R3) software and exported to Microsoft Excel for further processing. The basal activity of each mutant was estimated by averaging the raw BRET signals from the wells containing no agonist for a given mutant. BRET data at different agonist concentrations were presented as the difference between the raw BRET signal and the corresponding basal signal (ΔBRET). The ΔBRET values for different mutants were normalized by the maximal ΔBRET value for the WT receptor and expressed in percents. The resulting normalized ΔBRET % data were analyzed in GraphPad Prism (v. 10.0.2) using a nonlinear regression with the log(agonist) vs. response - (three parameters) analysis to produce the curves.

Statistical analysis. All statistical analysis was done using GraphPad Prism v. 10.0.2. For ONE-GO and TANGO concentration-response data sets, a nested one-way ANOVA test with Dunnett's multiple comparison correction relative to WT DP1 was conducted and used to calculate adjusted *P*-values of logEC50 and Emax values for nonlinear regression models. For expression and basal activity data sets, a one-way ANOVA test with Dunnett's multiple comparison correction relative to WT DP1 was employed.

Molecular dynamics (MD) simulations. All MD simulations were conducted with Gromacs[83] (v.2020.3) simulation engine under Charmm36 force-field parameters and topologies[84,85]. The initial coordinates were derived from the corresponding cryo-EM apo, active, and inactive state DP1 complexes; missing side-chains, mutations, and minor loops were restored to WT and optimized using the ICM-Pro[86] v.3.9-3a (Molsoft LLC) followed by structure regularization in the same software. The missing residues in cryo-EM models corresponding to the α-helical domain and a flexible loop (residues 257–262) of $G\alpha_s$ were not restored but, instead, were connected by flexible linkers across the gaps. All titratable residues were assigned charges corresponding to their dominant forms at physiological pH = 7.4, with one exception of $D72^{2.50}$. The carboxyl group of $D72^{2.50}$ side chain has been proposed to transition from charged to protonated neutral state upon receptor activation[68]. To test this hypothesis, we built two identical models of the active DP1-PGD2-G_s complexes using CHARMM-GUI: one with $D72^{2.50}$ deprotonated and one with $D72^{2.50}$ protonated. Each model was subjected to an independent set of MD simulations under identical settings.

The complete atomic systems for MD simulations were prepared with the CHARMM-GUI[87] interface (v.3.7). The molecular compositions of the systems are listed in Supplementary Table 6. The protein complexes were embedded in a lipid bilayer composed of 1,2-dipalmitoylphosphatidylcholine (DPPC), dioleoyl phosphatidylcholine (DOPC), or 1,2-palmitoyloleoylphasphatidylcholine (POPC), and cholesterol (CHL) at a ratio of DPPC:DOPC(or POPC):CHL = 0.55:0.15:0.30, referencing the setup used in GPCR simulations[88]. The systems were solvated with TIP3P water. All ligands were parameterized using the Ligand Reader & Modeler tool in the CHARMM-GUI[87] interface (v.3.7). Nine independent trajectories per each model were simulated starting from the corresponding initial system. After initial energy minimization, all systems were equilibrated for 60 ns, followed by production

runs of 1200 ns (1000 ns for the active state DP1-G_s complex with protonated D72$^{2.50}$) under NVT ensemble with V-rescale thermostat at 310 K (Supplementary Table 7). The simulations were performed on a GPU cluster at the Center for Advanced Research Computing (CARC) of the University of Southern California. MD trajectories were analyzed using MDTraj[89] and MDAnalysis[90] packages. Residue-based root mean square fluctuations (RMSF) and root mean square deviations (RMSD) for receptor and ligands are shown in Supplementary Figs. 23 and 24. Structural figures were prepared using ICM-Pro[86] v.3.9-3a.

Reporting summary

Further information on research design is available in the Nature Portfolio Reporting Summary linked to this article.

Data availability

Structure coordinates have been deposited in the Protein Data Bank (PDB) and cryo-EM density maps have been deposited in the Electron Microscopy Data Bank (EMDB) under the following accession codes: inactive state apo DP1$_{ICL3}$bRIL-BAG2-Nb: PDB 9EI5 and EMD-48077 (consensus map); inactive state ONO2550289-bound DP1$_{ICL3}$bRIL-BAG2-Nb: PDB 9EE5, EMD-47950 (composite map), EMD-71392 (consensus map), EMD-71379 (focused map #1, receptor), EMD-71393 (focused map #2, BAG2-Nb); inactive state ONO3030297-bound DP1$_{ICL3}$bRIL-BAG2-Nb: PDB 9EKH, EMD-48122 (composite map), EMD-71651 (consensus map), EMD-71656 (focused map #1, receptor), EMD-71657 (focused map #2, BAG2-Nb); active PGD2-bound DP1-Gs-Nb35: PDB 9E9S, EMD-47802 (composite map), EMD-71658 (consensus map), EMD-71659 (focused map #1, receptor), EMD-71660 (focused map #2, Gs-Nb35); active BW245C-bound DP1-Gs-Nb35: PDB 9AU0, EMDB-43839 [https://www.ebi.ac.uk/pdbe/entry/emdb/EMD-43839] (composite map), EMD-71661 (consensus map), EMD-71662 (focused map #1, receptor), EMD-71663 (focused map #2, Gs-Nb35). Atomic coordinates for previously determined structures can be accessed via accession codes: 2RH1, 3SN6, 5YWY, 5YHL, 6AK3, 6M9T, 6IIU, 6IIV, 7CX2, 6WW2, 7CX3, 7CX4, 7D7M, 7WU9, 8GCM, 8GCP, 8GD9, 8GDA, 8GDB, 8GDC, 8IQ4, 8IQ6, 8IUK, 8IUL, 8IUM, 8X79, 8X7A, 8XJK, 8XJL, 8XJM, 8XJN, 8XJO. MD trajectories have been deposited to Zenodo under accession codes 15278219 (active, inactive, and apo states) and 15391966 (active state with protonated D72$^{2.50}$). Source Data are provided as a Source data file. Source data are provided with this paper.

References

1. Urade, Y. & Hayaishi, O. Prostaglandin D2 and sleep/wake regulation. *Sleep. Med. Rev.* **15**, 411–418 (2011).
2. Ueno, R. et al. Role of prostaglandin D2 in the hypothermia of rats caused by bacterial lipopolysaccharide. *Proc. Natl Acad. Sci. USA* **79**, 6093–6097 (1982).
3. Uda, R., Horiguchi, S., Ito, S., Hyodo, M. & Hayaishi, O. Nociceptive effects induced by intrathecal administration of prostaglandin D2, E2 or F2α to conscious mice. *Brain Res.* **510**, 26–32 (1990).
4. Matsuoka, T. et al. Prostaglandin D2 as a mediator of allergic asthma. *Science* **287**, 2013–2017 (2000).
5. Braune, S., Kupper, J.-H. & Jung, F. Effect of prostanoids on human platelet function: an overview. *Int. J. Mol. Sci.* **21**, 9020 (2020).
6. Nagoshi, H. et al. Prostaglandin D2 inhibits inducible nitric oxide synthase expression in rat vascular smooth muscle cells. *Circ. Res.* **82**, 204–209 (1998).
7. Pettipher, R., Hansel, T. T. & Armer, R. Antagonism of the prostaglandin D2 receptors DP1 and CRTH2 as an approach to treat allergic diseases. *Nat. Rev. Drug Discov.* **6**, 313–325 (2007).
8. Matsuoka, T. & Narumiya, S. Prostaglandin receptor signaling in disease. *ScientificWorldJournal* **7**, 1329–1347 (2007).
9. Claar, D., Hartert, T. V. & Peebles, R. S. Jr The role of prostaglandins in allergic lung inflammation and asthma. *Expert Rev. Respir. Med.* **9**, 55–72 (2015).
10. Nagata, K. et al. CRTH2, an orphan receptor of T-helper-2-cells, is expressed on basophils and eosinophils and responds to mast cell-derived factor (s). *FEBS Lett.* **459**, 195–199 (1999).
11. Moon, T. C. et al. Expression of DP2 (CRTh2), a prostaglandin D2 receptor, in human mast cells. *PLoS ONE* **9**, e108595 (2014).
12. Tait Wojno, E. et al. The prostaglandin D2 receptor CRTH2 regulates accumulation of group 2 innate lymphoid cells in the inflamed lung. *Mucosal Immunol.* **8**, 1313–1323 (2015).
13. Wlodawer, P. & Samuelsson, B. On the organization and mechanism of prostaglandin synthetase. *J. Biol. Chem.* **248**, 5673–5678 (1973).
14. Smith, W. L., DeWitt, D. L. & Garavito, R. M. Cyclooxygenases: structural, cellular, and molecular biology. *Annu. Rev. Biochem.* **69**, 145–182 (2000).
15. FitzGerald, G. A. & Patrono, C. The coxibs, selective inhibitors of cyclooxygenase-2. *N. Engl. J. Med.* **345**, 433–442 (2001).
16. Breyer, R. M., Baghassarian, C. K., Myers, S. A. & Breyer, M. D. Prostanoid receptors: subtypes and signaling. *Annu. Rev. Pharmacol. Toxicol.* **41**, 661–690 (2001).
17. Nagata, K. & Hirai, H. The second PGD2 receptor CRTH2: structure, properties, and functions in leukocytes. *Prostaglandins Leukot. Essent. Fat. Acids* **69**, 169–177 (2003).
18. Holgate, S. T., Burns, G., Robinson, C. & Church, M. Anaphylactic- and calcium-dependent generation of prostaglandin D2 (PGD2), thromboxane B2, and other cyclooxygenase products of arachidonic acid by dispersed human lung cells and relationship to histamine release. *J. Immunol.* **133**, 2138–2144 (1984).
19. Gundel, R. H. et al. Antigen-induced mediator release in primates. *Am. Rev. Respir. Dis.* **144**, 78–82 (1991).
20. Murray, J. J. et al. Release of prostaglandin D2 into human airways during acute antigen challenge. *N. Engl. J. Med.* **315**, 800–804 (1986).
21. Werder, R. B. et al. PGD2/DP2 receptor activation promotes severe viral bronchiolitis by suppressing IFN-λ production. *Sci. Transl. Med.* **10**, eaao0052 (2018).
22. Rittchen, S. & Heinemann, A. Therapeutic potential of hematopoietic prostaglandin D2 synthase in allergic inflammation. *Cells* **8**, 619 (2019).
23. Hardy, C. C., Robinson, C., Tattersfield, A. E. & Holgate, S. T. The bronchoconstrictor effect of inhaled prostaglandin D2 in normal and asthmatic men. *N. Engl. J. Med.* **311**, 209–213 (1984).
24. Van Ly, D. et al. Characterising the mechanism of airway smooth muscle β2 adrenoceptor desensitization by rhinovirus infected bronchial epithelial cells. *PloS ONE* **8**, e56058 (2013).
25. Hammad, H. et al. Activation of the D prostanoid 1 receptor suppresses asthma by modulation of lung dendritic cell function and induction of regulatory T cells. *J. Exp. Med.* **204**, 357–367 (2007).
26. Kupczyk, M. & Kuna, P. Targeting the PGD 2/CRTH2/DP1 signaling pathway in asthma and allergic disease: current status and future perspectives. *Drugs* **77**, 1281–1294 (2017).
27. Angeli, V. et al. Activation of the D prostanoid receptor 1 regulates immune and skin allergic responses. *J. Immunol.* **172**, 3822–3829 (2004).
28. Idzko, M. et al. Inhaled iloprost suppresses the cardinal features of asthma via inhibition of airway dendritic cell function. *J. Clin. Invest.* **117**, 464–472 (2007).
29. Whittle, B. J., Silverstein, A. M., Mottola, D. M. & Clapp, L. H. Binding and activity of the prostacyclin receptor (IP) agonists, treprostinil and iloprost, at human prostanoid receptors: treprostinil is a potent DP1 and EP2 agonist. *Biochem. Pharmacol.* **84**, 68–75 (2012).
30. Li, F. et al. Prostaglandin E1 and its analog misoprostol inhibit human CML stem cell self-renewal via EP4 receptor activation and repression of AP-1. *Cell Stem Cell* **21**, 359–373.e5 (2017).
31. Xiang, J. et al. Successful strategies to determine high-resolution structures of GPCRs. *Trends Pharmacol. Sci.* **37**, 1055–1069 (2016).
32. Guo, Q. et al. A method for structure determination of GPCRs in various states. *Nat. Chem. Biol.* **20**, 74–82 (2024).

33. Zhang, M. et al. G protein-coupled receptors (GPCRs): advances in structures, mechanisms, and drug discovery. *Signal Transduct. Target. Ther.* **9**, 88 (2024).
34. Zhang, K., Wu, H., Hoppe, N., Manglik, A. & Cheng, Y. Fusion protein strategies for cryo-EM study of G protein-coupled receptors. *Nat. Commun.* **13**, 4366 (2022).
35. Zhang, X. et al. Evolving cryo-EM structural approaches for GPCR drug discovery. *Structure* **29**, 963–974.e6 (2021).
36. Shihoya, W., Iwama, A., Sano, F. K. & Nureki, O. Cryo-EM advances in GPCR structure determination. *J. Biochem.* **176**, 1–10 (2024).
37. Qu, C. et al. Ligand recognition, unconventional activation, and G protein coupling of the prostaglandin E2 receptor EP2 subtype. *Sci. Adv.* **7**, eabf1268 (2021).
38. Audet, M. et al. Crystal structure of misoprostol bound to the labor inducer prostaglandin E2 receptor. *Nat. Chem. Biol.* **15**, 11–17 (2019).
39. Morimoto, K. et al. Crystal structure of the endogenous agonist-bound prostanoid receptor EP3. *Nat. Chem. Biol.* **15**, 8–10 (2019).
40. Suno, R. et al. Structural insights into the G protein selectivity revealed by the human EP3-Gi signaling complex. *Cell Rep.* **40**, 111323 (2022).
41. Huang, S.-M. et al. Single hormone or synthetic agonist induces Gs/Gi coupling selectivity of EP receptors via distinct binding modes and propagating paths. *Proc. Natl Acad. Sci. USA* **120**, e2216329120 (2023).
42. Nojima, S. et al. Cryo-EM structure of the prostaglandin E receptor EP4 coupled to G protein. *Structure* **29**, 252–260.e6 (2021).
43. Lv, X. et al. Structures of human prostaglandin F2α receptor reveal the mechanism of ligand and G protein selectivity. *Nat. Commun.* **14**, 8136 (2023).
44. Wu, C. et al. Ligand-induced activation and G protein coupling of prostaglandin F2α receptor. *Nat. Commun.* **14**, 2668 (2023).
45. Li, X. et al. Structural basis for ligand recognition and activation of the prostanoid receptors. *Cell Rep.* **43**, 113893 (2024).
46. Wang, J. J. et al. Molecular recognition and activation of the prostacyclin receptor by anti-pulmonary arterial hypertension drugs. *Sci. Adv.* **10**, eadk5184 (2024).
47. Xu, J. et al. Molecular basis of lipid and ligand regulation of prostaglandin receptor DP2. *Proc. Natl Acad. Sci. USA* **121**, e2403304121 (2024).
48. Fan, H. et al. Structural basis for ligand recognition of the human thromboxane A2 receptor. *Nat. Chem. Biol.* **15**, 27–33 (2019).
49. Toyoda, Y. et al. Ligand binding to human prostaglandin E receptor EP4 at the lipid-bilayer interface. *Nat. Chem. Biol.* **15**, 18–26 (2019).
50. Wang, L. et al. Structures of the human PGD2 receptor CRTH2 reveal novel mechanisms for ligand recognition. *Mol. Cell* **72**, 48–59.e4 (2018).
51. Liu, H. et al. Molecular basis for lipid recognition by the prostaglandin D2 receptor CRTH2. *Proc. Natl Acad. Sci. USA* **118**, e2102813118 (2021).
52. Chun, E. et al. Fusion partner toolchest for the stabilization and crystallization of G protein-coupled receptors. *Structure* **20**, 967–976 (2012).
53. Ballesteros, J. A. & Weinstein, H. [19] Integrated methods for the construction of three-dimensional models and computational probing of structure-function relations in G protein-coupled receptors. *Methods Neurosci.* **25**, 366–428 (1995).
54. Janicot, R. et al. Direct interrogation of context-dependent GPCR activity with a universal biosensor platform. *Cell* **187**, 1527–1546 (2024).
55. Raskovalov, A., Kim, D. & Cherezov, V. ONE-GO: direct detection of context-dependent GPCR activity. *Cell Res* **34**, 543–544 (2024).
56. Mukherjee, S. et al. Synthetic antibodies against BRIL as universal fiducial marks for single-particle cryoEM structure determination of membrane proteins. *Nat. Commun.* **11**, 1598 (2020).
57. Tsutsumi, N. et al. Structure of human Frizzled5 by fiducial-assisted cryo-EM supports a heterodimeric mechanism of canonical Wnt signaling. *eLife* **9**, e58464 (2020).
58. Ereño-Orbea, J. et al. Structural basis of enhanced crystallizability induced by a molecular chaperone for antibody antigen-binding fragments. *J. Mol. Biol.* **430**, 322–336 (2018).
59. Zhou, Q. et al. Common activation mechanism of class A GPCRs. *eLife* **8**, e50279 (2019).
60. Liu, W. et al. Structural basis for allosteric regulation of GPCRs by sodium ions. *Science* **337**, 232–236 (2012).
61. Katritch, V. et al. Allosteric sodium in class A GPCR signaling. *Trends Biochem. Sci.* **39**, 233–244 (2014).
62. Zarzycka, B., Zaidi, S. A., Roth, B. L. & Katritch, V. Harnessing ion-binding sites for GPCR pharmacology. *Pharmacol. Rev.* **71**, 571–595 (2019).
63. Liang, Y.-L. et al. Phase-plate cryo-EM structure of a biased agonist-bound human GLP-1 receptor-Gs complex. *Nature* **555**, 121–125 (2018).
64. Rasmussen, S. G. et al. Crystal structure of the β2 adrenergic receptor–Gs protein complex. *Nature* **477**, 549–555 (2011).
65. Zhang, C. et al. High-resolution crystal structure of human protease-activated receptor 1. *Nature* **492**, 387–392 (2012).
66. Cheng, R. K. Y. et al. Structural insight into allosteric modulation of protease-activated receptor 2. *Nature* **545**, 112–115 (2017).
67. Luginina, A. et al. Structure-based mechanism of cysteinyl leukotriene receptor inhibition by antiasthmatic drugs. *Sci. Adv.* **5**, aax2518 (2019).
68. Vickery, O. N. et al. Intracellular transfer of Na+ in an active-state G-protein-coupled receptor. *Structure* **26**, P171–180.E2 (2018).
69. Flock, T. et al. Universal allosteric mechanism for Gα activation by GPCRs. *Nature* **524**, 173–179 (2015).
70. Cherezov, V. et al. High-resolution crystal structure of an engineered human beta2-adrenergic G protein-coupled receptor. *Science* **318**, 1258–1265 (2007).
71. Kroeze, W. K. et al. PRESTO-Tango as an open-source resource for interrogation of the druggable human GPCRome. *Nat. Struct. Mol. Biol.* **22**, 362–369 (2015).
72. Smyth, E. M., Grosser, T., Wang, M., Yu, Y. & FitzGerald, G. A. Prostanoids in health and disease. *J. Lipid Res.* **50**, S423–S428 (2009).
73. Naganawa, A. et al. Carboxylic acid compounds and medicinal compositions containing the same as the active ingredient. Patent WO2005028455A1 (2004).
74. Zheng, S. Q. et al. MotionCor2: anisotropic correction of beam-induced motion for improved cryo-electron microscopy. *Nat. Methods* **14**, 331–332 (2017).
75. Punjani, A. et al. CryoSPARC: algorithms for rapid unsupervised cryo-EM structure determination. *Nat. Methods* **14**, 290–296 (2017).
76. Bepler, T. et al. Positive-unlabeled convolutional neural networks for particle picking in cryo-electron micrographs. *Nat. Methods* **16**, 1153–1160 (2019).
77. Liebschner, D. et al. Macromolecular structure determination using X-rays, neutrons and electrons: recent developments in phenix. *Acta Crystallogr. D. Struct. Biol.* **75**, 861–877 (2019).
78. Jumper, J. et al. Highly accurate protein structure prediction with AlphaFold. *Nature* **596**, 583–589 (2021).
79. Meng, E. C. et al. UCSF ChimeraX: tools for structure building and analysis. *Prot. Sci.* **32**, e4792 (2023).
80. Emsley, P., Lohkamp, B., Scott, W. G. & Cowtan, K. Features and development of Coot. *Acta Crystallogr. D. Biol. Crystallogr.* **66**, 486–501 (2010).
81. Barnea, G. et al. The genetic design of signaling cascades to record receptor activation. *Proc. Natl Acad. Sci. USA* **105**, 64–69 (2008).

82. Liu, H. et al. Prostaglandin D_2 toxicity in primary neurons is mediated through its bioactive cyclopentenone metabolites. *Neurotoxicology* **39**, 35–44 (2013).
83. Abraham, M. J. et al. GROMACS: high performance molecular simulations through multi-level parallelism from laptops to supercomputers. *SoftwareX* **1**, 19–25 (2015).
84. Huang, J. et al. CHARMM36m: an improved force field for folded and intrinsically disordered proteins. *Nat. Methods* **14**, 71–73 (2017).
85. Kim, S. et al. CHARMM-GUI ligand reader and modeler for CHARMM force field generation of small molecules. *J. Comput. Chem.* **38**, 1879–1886 (2017).
86. Abagyan, R., Totrov, M. & Kuznetsov, D. ICM—a new method for protein modeling and design: applications to docking and structure prediction from the distorted native conformation. *J. Comput. Chem.* **15**, 488–506 (1994).
87. Jo, S., Kim, T., Iyer, V. G. & Im, W. CHARMM-GUI: a web-based graphical user interface for CHARMM. *J. Comput. Chem.* **29**, 1859–1865 (2008).
88. Leonard, A. N. & Lyman, E. Activation of G-protein-coupled receptors is thermodynamically linked to lipid solvation. *Biophys. J.* **120**, 1777–1787 (2021).
89. McGibbon, R. T. et al. MDTraj: a modern open library for the analysis of molecular dynamics trajectories. *Biophys. J.* **109**, 1528–1532 (2015).
90. Michaud-Agrawal, N., Denning, E. J., Woolf, T. B. & Beckstein, O. MDAnalysis: a toolkit for the analysis of molecular dynamics simulations. *J. Comput. Chem.* **32**, 2319–2327 (2011).

Acknowledgements

We thank Martin Audet for conducting initial construct design for DP1, Benjamin Stauch for suggesting stabilizing mutations, Kelly Villers for help with protein expression, Jayden Salve for assisting with assays, and Katya Kadyshevskaya for help with illustrations. Cryo-EM data were collected at the Stanford-SLAC Cryo-EM Center (S2C2) supported by the National Institutes of Health Common Fund Transformative High-Resolution Cryo-Electron Microscopy program (U24 GM129541) and at the Center of Excellence in NanoImaging (CNI) at the University of Southern California. We acknowledge the Center for Advanced Research Computing (CARC) of the University of Southern California for providing computational resources for MD simulations. This work was supported by the National Institutes of Health grants R35GM127086 (V.C.) and R35GM153437 (V.K.).

Author contributions

B.D., V.K., and V.C. conceived the project, B.D. prepared samples, collected and processed cryo-EM data, D.K. processed cryo-EM data, B.D., G.W.H., and V.C. refined structures, A.R. and H.K. conducted assays, W.L., J.H.L., and V.K. performed and analyzed MD simulations, B.D., W.L., V.K., and V.C. prepared initial draft, all authors edited the paper.

Competing interests

The authors declare no competing interests.

Additional information

Supplementary information The online version contains supplementary material available at https://doi.org/10.1038/s41467-025-64002-z.

Correspondence and requests for materials should be addressed to Vsevolod Katritch or Vadim Cherezov.

Peer review information *Nature Communications* thanks Giuseppe Deganutti, Sanduo Zheng, and the other, anonymous, reviewer for their contribution to the peer review of this work. A peer review file is available.